COSMOLOGICAL IMPLICATIONS OF MODIFIED GRAVITY: SPHERICAL COLLAPSE AND HIGHER ORDER CORRELATIONS

Alexander Borisov

A DISSERTATION

in

Physics and Astronomy

Presented to the Faculties of the University of Pennsylvania

in Partial Fulfillment of the Requirements for the Degree of Doctor of Philosophy

2009

Supervisor of Dissertation

Bhuvnesh Jain
Professor of Physics and Astronomy

Graduate Group Chairperson

Ravi Sheth, Professor of Physics and Astronomy

Dissertation Committee
Masao Sako, Assistant Professor of Physics and Astronomy
Mark Trodden, Professor of Physics and Astronomy
Hugh H. Williams, Professor of Physics and Astronomy

Abstract

COSMOLOGICAL IMPLICATIONS OF MODIFIED GRAVITY: SPHERICAL COLLAPSE AND HIGHER ORDER CORRELATIONS

Alexander Borisov

Bhuvnesh Jain

In the Standard Model of Cosmology the nature of the Dark Energy has become one of the most significant and conceptual challenges to be resolved. One of the possible approaches to solving it is to introduce modifications to General Relativity, that include Chameleon effects, which allow for a change in the strength of gravity based on the environment. This can provide for a consistent explanation of both large-scale observations and Solar system experiments. In the task to distinguish them from the ΛCDM model of gravity, or any other competing explanation, we need to study the consequences of these modifications for the growth of perturbations. In this thesis a recently developed Chameleon $f(R)$ modification to gravity is explored. We study its consequences for the distribution of matter on large scale using the Bispectrum. Using $1D$ simulations we examine the formation of galaxy and cluster halos and its observational effects. Finally we present an investigation of a method for studying gravitational lensing.

Contents

List of Tables

List of Figures

Chapter 1

Introduction

1.1 Dark energy and the need for modified gravity

The last decade has been an active period in the evolution of our understanding of the Universe. The scientific community has achieved significant advancement in analyzing and measuring its content, and a variety of new experiments are underway or being developed to reduce the uncertainty of our measurements, or to resolve the remaining debates. Like high-energy physics, cosmology has its own Standard Model. According to it [1] the Universe is a spatially flat - that is, the energy density contained in the curvature of space is negligible. It contains about 4% baryonic matter, 23% Cold Dark Matter (CDM) and the remaining 73% in the so called Dark Energy, which many consider to be the cosmological constant driving the acceleration of the Universe. The present value of the Hubble constant is $H_0 = 71\,\mathrm{km/s/Mpc}$.

The great unknown in the Standard Model of Cosmology, however, is the nature of the Dark Energy. It has become one of the most significant and conceptual challenges

that modern physics has to face. While we are waiting for a successful quantization of gravitation theories – for example string theory – the classical paradigm is that gravity is the geometry of space-time in which matter propagates. In the evolving research process two general approaches have emerged. One is to look for a solution in the matter sector of the paradigm – Dark Energy is a new unseen form of energy which has negative pressure. The other is to modify the geometry part via changes in the Einstein-Hilbert action.

The accepted gravitational theory, General Relativity (GR), is a field theory described by a 2-tensor called the metric tensor $g_{\mu\nu}$. The aforementioned action then is:

$$S = S_g + S_m = \left[\frac{1}{16\pi G}\int d^4x\sqrt{-g}R\right] + S_m, \tag{1.1}$$

where g is the determinant of the metric tensor, and R is the Ricci scalar, constructed by the metric and its derivatives, and S_m is the part of the action describing the matter content of the Universe. Varying this action leads to the well-known field equations - the Einstein equation:

$$R_{\mu\nu} - \frac{1}{2}Rg_{\mu\nu} = 8\pi G T_{\mu\nu} \tag{1.2}$$

Unfortunately General Relativity in this form cannot explain the observed accelerated expansion of the Universe. The task of modifying the Einstein-Hilbert action is by itself not trivial and there are many approaches to it. Let us first consider some implications of General Relativity. When we look at the Universe at very large scales we observe that it is homogeneous and isotropic and thus is suitably described by the so called Friedmann-Robertson-Walker metric:

$$ds^2 = -dt^2 + a^2(t)(dr^2 + r^2 d\Omega^2), \tag{1.3}$$

where we have used the observation that the Universe is spatially flat. The quantity $a(t)$ is called the scale factor. In this case the so called Friedmann equation can be derived:

$$H^2(t) \equiv \left(\frac{\dot{a}}{a}\right)^2 = \frac{8\pi G\rho}{3} \tag{1.4}$$

where $H(t)$ describes the evolution of the Hubble parameter and $\rho(t)$ is the total mass density. We can also define the deceleration parameter:

$$q \equiv -\frac{\dot{H}}{H^2} - 1 = -\frac{\ddot{a}a}{\dot{a}^2} \tag{1.5}$$

This dimensionless paramater can be negative, i.e. the Universe is accelerating, for some unusual type of energy-matter species. The deceleration can be expressed via its density and pressure as:

$$q = \frac{1}{2}\left(1 + 3\frac{p}{\rho}\right) \tag{1.6}$$

and after introducing the equation of state for that species $p = w\rho$:

$$q = \frac{1}{2}\left(1 + 3w\right) \tag{1.7}$$

As mentioned, the observations [2] require that q becomes negative sometime in the evolution of the Universe. This means that a species for which $w < -\frac{1}{3}$ should dominate at late times. The problem thus is that no known particle, including candidate particles that constitute CDM, has such an equation of state. In particular CDM has pressure of zero or $w = 0, q = \frac{1}{2}$.

We can gain some intuition by simply adding a constant term to the action:

$$S_g = \frac{1}{16\pi G}\int d^4x\sqrt{-g}(R - \Lambda) \tag{1.8}$$

This then leads to a modification in the Einstein equations:

$$R_{\mu\nu} - \frac{1}{2}Rg_{\mu\nu} = 8\pi G T_{\mu\nu} + \Lambda g_{\mu\nu} \tag{1.9}$$

By looking at the new term it becomes clear that in a flat universe it represents the Stress tensor for an energy species in the form:

$$T^{\mu}_{\nu} = diag(\Lambda, \Lambda, \Lambda, \Lambda). \tag{1.10}$$

But this means that it has $w = -1$. Thus we have resolved the issue with the acceleration of the Universe at late times, when the cosmological constant starts dominating over the matter content. But just adding *ad hoc* a cosmological constant to the action, or invoking the anthropic principle, seems theoretically unappealing. One could argue that quantum field theories predict a huge cosmological constant from the energy of the quantum vacuum. But the measured cosmological constant from observations is:

$$\rho_{\Lambda} \backsimeq 10^{-47}\,\mathrm{GeV}^4, \tag{1.11}$$

while the field theory prediction is of order of the Plank mass ${\mathrm{M_{Pl}}}^4$:

$$\rho_{\Lambda,QFT} \backsimeq 10^{72}\,\mathrm{GeV}^4. \tag{1.12}$$

This discrepancy of about 120 orders of magnitude is catastrophic. Aside from this prediction, particle physics has yet to pinpoint the origin of Cold Dark Matter and is very far from considering exotic particles with negative pressure.

In the meantime further modifications of the Einstein-Hilbert action are being explored. Some borrow ideas from string theory and create braneworld cosmologies. A particular example is the DGP model which has seen a lot of development recently [3, 4, 5]. In it we live on a particular slice of the bulk space-time called a brane. The overall action when restricted to the brane with proper boundary conditions will produce a modified Friedmann equation:

$$H^2 - \frac{H}{r_0} = \frac{8\pi G}{3}\rho, \tag{1.13}$$

which depending on the choice of the r_0 parameter produces an accelerating Universe at late times when $\frac{H}{r_0} \approx \frac{8\pi G}{3}\rho$. Recently there has been a lot of debate over the viability of DGP models [6] but the work continues to overcome these obstacles.

Another approach is to consider empirical modifications of the Einstein-Hilbert action (similar to just adding *ad hoc* cosmological constant) with the reasoning that they could be viewed as the effective low-energy Lagrangians of some higher dimensional string theory model. Of particular interest are the so called $f(R)$ modifications:

$$S_g = \frac{1}{16\pi G}\int d^4x\sqrt{-g}(R + f(R)), \tag{1.14}$$

where $f(R)$ is a function of the Ricci scalar [7]. A major obstacle for such theories has been that they could not consistently explain both large-scale observations and Solar System experiments. On the other hand, in a somewhat unrelated way a new mechanism was proposed [8] which allowed for a change in the strength of gravity based on the environment/local conditions. This was called the Chameleon mechanism and quickly became a powerful tool for adjusting the behavior of models on small scales. The model proposed by Hu and Sawiki [9] in 2007 exhibited such Chameleon properties and is the model studied in this dissertation. This model is designed to fit the same expansion history as the Standard Model of cosmology – ΛCDM – to agree with the observations. Like all other modifications of gravity, it depends on several parameters that can be adjusted according to experimental data. How do we distinguish the new hypothesis from the ΛCDM model or any other competing explanations of the observed phenomena? The answer is conceptually simple: study what consequences and predictions the proposed hypothesis leads to, then compare them to experimental data, or propose new experiments designed to test the predictions [10]. The consequences of the selected model we have

studied are: matter distribution statistics on large scales and the formation of halos and clusters.

1.2 Matter distribution statistics: the Bispectrum

In the study of matter statistics there are two approaches: perturbation theory (valid in the quasi-linear regime) and simulations (necessary to explore the non-linear regime). We carried out a perturbative calculation of the three-point statistic: the Bispectrum.

In perturbation theory we start with an ansatz for the metric described by two scalar potentials in Newtonian gauge:

$$ds^2 = -(1-2\Psi)\ dt^2 + (1-2\Phi)\ a^2(t)\ d\vec{x}^2, \tag{1.15}$$

where in GR the two potentials will generally be equal to each other (in the absence of anisotropic stresses): $\Phi = -\Psi$. It is very convenient to express all quantities in Fourier space, such as the overdensity:

$$\hat{\delta}(\vec{k},t) = \int d^3x\ \delta(\vec{x},t)\ e^{-i\vec{k}\cdot\vec{x}} \tag{1.16}$$

Using the continuity, Euler, and Poisson's equations we can arrive at the following equations, which describe the evolution of the overdensity and the connection between the scalar potentials and the matter distribution:

$$\ddot{\delta} + 2H\dot{\delta} + \frac{k^2\Psi}{a} = 0. \tag{1.17}$$

$$k^2(\Phi - \Psi) = -8\pi\tilde{G}_{\rm eff}(k,t)\bar{\rho}_{\rm MG}a^2\delta(k,t) \tag{1.18}$$

$$\Phi = -\Psi\ \eta(k,t) \tag{1.19}$$

where $\tilde{G}_{\rm eff} = G_{\rm eff}(1+\eta^{-1})/2$. The parameters $\tilde{G}_{\rm eff}$ and $\eta(k,t)$ are sufficient to describe general modifications to gravity in perturbation theory. Now expanding the density perturbations, $\delta(\vec{k},t) \simeq \delta_{initial}(\vec{k})D(k,t)$, we obtain the equation for the linear growth factor:

$$\ddot{D} + 2H\dot{D} - \frac{8\pi\tilde{G}_{\rm eff}}{(1+\eta)}\bar{\rho}a^2 \; D = 0. \tag{1.20}$$

For particular choice of $\tilde{G}_{\rm eff}$ and $\eta(k,t)$ based on our model of modified gravity we will obtain a first order solution for the overdensity field. Furthermore, we will later show how to obtain a second order perturbative solution, as it is needed for the calculation of the Bispectrum.

As already mentioned, the 2-point correlation function – the power spectrum – has been studied in the literature [9]. We will instead focus on the 3-point correlation function of the density field:

$$\langle\delta(\vec{k}_1)\delta(\vec{k}_2)\delta(\vec{k}_3)\rangle = (2\pi)^3\delta_{\rm D}(\vec{k}_1+\vec{k}_2+\vec{k}_3)B_\delta(\vec{k}_1,\vec{k}_2,\vec{k}_3) \tag{1.21}$$

Observe that for an initially Gaussian density field we have $B_\delta \sim \langle\delta^3\rangle \sim \langle\delta_1^2\delta_2\rangle$, which is where we need the second order solution. Additionally, since $\delta_2 \propto O(\delta_1^2)$, the Bispectrum is proportional to the second power of the power spectrum. To scale out the amplitude of the power spectrum we are also interested in the so called reduced Bispectrum:

$$Q_\delta \equiv \frac{B_\delta(\vec{k}_1,\vec{k}_2,\vec{k}_3)}{P_\delta(k_1)P_\delta(k_2)+P_\delta(k_2)P_\delta(k_3)+P_\delta(k_1)P_\delta(k_3)}. \tag{1.22}$$

Detailed derivations, results and discussion of our calculations of the Bispectrum will be provided in Chapter 2 of this thesis.

1.3 Structure Formation and Gravitational Lensing

To provide more tools for exploring modifications of gravity, the formation of large-scale structure can be studied. Dark matter halos are the basic building blocks of the Universe. A study of their properties (density profiles, halo mass function etc.) to see how they differ when compared to the predictions of ΛCDM gravity will be helpful in guiding the direction of observational surveys. A common approach in this field is to investigate the evolution of an isotropic initial overdensity – the spherical collapse. While this simple case can be solved analytically in the Standard Model, such solutions can not be obtained for general modifications of gravity. For the particular case of $f(R)$ modification that is the topic of this thesis, analytical solutions can be obtained in two limiting approximations [11]. This is the reason that, for a more detailed study, simulations are needed. The task is further complicated by having to concurrently simulate the evolution of the scalar field associated with the $f(R)$ model [12]. The details of our simulation, the technical difficulties, and current results are described in Chapter 3.

An important consequence of the previous considerations is that modifications to gravity affect the evolution of the matter content of the Universe, which is mostly Cold Dark Matter. Recently a powerful tool has been developed, that allows us a direct observation of the distribution of CDM – gravitational lensing. Matter distribution corresponds to perturbations in the metric, which in turn causes perturbations to the null-geodesics, the light paths. When light from a galaxy passes through a massive object its image can appear distorted; its size and shape will change, corresponding to magnificaton and shear. Weak gravitational lensing uses the statistical properties of the shapes of many such distorted galaxies to obtain information about the foreground dark matter, which acts as a

lens. The basics of weak lensing are outlined in [13].

Improvements in the methods used in studying gravitational lensing are essential for furthering our understanding of cosmology. A study of optimizing techniques for measuring galaxy shapes for lensing was done in [14]. In Chapter 4 we present an investigation of a particular calculation in the statistical measurement of galaxy shapes, the evaluation of the Responsivity.

Chapter 2

The Bispectrum in the quasi-linear regime

2.1 Introduction

The energy contents of the universe pose an interesting puzzle, in that general relativity (GR) plus the Standard Model of particle physics can only account for about 4% of the energy density inferred from observations. By introducing dark matter and dark energy, which account for the remaining 96% of the total energy budget of the universe, cosmologists have been able to account for a wide range of observations, from the overall expansion of the universe to the large scale structure of the early and late universe [15].

The dark matter/dark energy scenario assumes the validity of GR at galactic and cosmological scales and introduces exotic components of matter and energy to account for observations. Since GR has not been tested independently on these scales, a natural alternative is that GR itself needs to be modified on large scales. This possibility, that

modifications in GR on galactic and cosmological scales can replace dark matter and/or dark energy, has become an area of active research in recent years.

Attempts have been made to modify GR with a focus on galactic [16] or cosmological scales [3, 7, 17]. Modified Newtonian Dynamics (MOND) and its relativistic version (Tensor-Vector-Scalar, TeVeS) [16] attempt to explain observed galaxy rotation curves without dark matter (but have problems on larger scales). The DGP model [3], in which gravity lives in a 5D brane world, naturally leads to late time acceleration of the universe.

Adding a correction term $f(R)$ to the Einstein-Hilbert action [7] also allows late time acceleration of the universe to be realized.

In this paper we will focus on modified gravity (MG) theories that are designed as an alternative to dark energy to produce the present day acceleration of the universe. In these models, such as DGP and $f(R)$ models, gravity at late cosmic times and on large-scales departs from the predictions of GR. By design, successful MG models are difficult to distinguishable from viable DE models against observations of the expansion history of the universe. However, in general they predict a different growth of perturbations which can be tested using observations of large-scale structure (LSS) [4, 18, 19, 20, 21, 22, 23, 24, 25, 26, 27, 28, 29, 30, 31, 32].

In this chapter we consider the quasilinear regime of clustering in which perturbation theory calculations are valid. We explore what $f(R)$ modifications to gravity predict about the behavior of the three-point correlation function. In §II we outline the particular type of $f(R)$ gravity model we will be using for our calculations. In §III we introduce the fundamentals of perturbation theory and in particular how it applies to modified gravity.

In §IV we focus on second order corrections and in particular the Bispectrum. In §V we present our results and compare with other studies of the nonlinear regime. In §VI we discuss the implications for observations.

2.2 The $f(R)$ modified gravity model

In general $f(R)$ models are a modification of the Einstein-Hilbert action of the form:

$$S = \int d^4x\sqrt{-g}\left[\frac{R + f(R)}{2\kappa^2} + \mathcal{L}_m\right], \tag{2.1}$$

where R is the curvature, $\kappa^2 = 8\pi G$, and $\mathcal{L}_m$ is the matter Lagrangian. A major issue with gravity modifications has been that while they are successful at explaining the acceleration of the universe, they also tend to fail to comply with Solar system (very small scales) observations. Recently, though, the so called Chameleon mechanism was found [33, 8] that makes it possible to overcome this problem. Significant attempts have been made to include Chameleon behavior [5] in DGP theories as well. One example of an $f(R)$ model that exhibits Chameleon behavior was constructed by Hu and Sawicki [9]. The functional form of $f(R)$ there is derived from a list of observational requirements: it should mimic ΛCDM in the high-redshift regime as well as produce ΛCDM acceleration of the universe at low redshift without a true cosmological constant; it should also fit Solar system observations.

The particular form chosen by [9] is:

$$f(R) = -m^2\frac{c_1(R/m^2)^n}{c_2(R/m^2)^n + 1} \tag{2.2}$$

with

$$m^2 \equiv \frac{\kappa^2 \bar{\rho}_0}{3} = (8315 Mpc)^{-2} \left(\frac{\Omega_m h^2}{0.13} \right) \tag{2.3}$$

where $\kappa^2 \equiv 8\pi G$ and $\bar{\rho}_0$ is the average density today. In this model, modifications to GR only appear at low redshift, when we are safely in the matter dominated regime. The properties of the model are well described by the auxiliary scalar field $f_R \equiv \frac{df(R)}{dR}$.

Before going to the expansion history, it is worth briefly reviewing the main features of this model, following the original presentation in [9]. The trace of the modified Einstein equations serves as the equation of motion for f_R:

$$3\Box f_R - R + f_R R - 2f = -\kappa^2 \rho, \tag{2.4}$$

or, in terms of the effective potential,

$$\Box f_R = \frac{\partial V_{\text{eff}}}{\partial f_R}. \tag{2.5}$$

The effective mass for the f_R field is then given by the second derivative of V_{eff}, evaluated at its extremum:

$$m_{\text{eff}}^2 = \frac{\partial^2 V_{\text{eff}}}{\partial f_R^2} = \frac{1}{3} \left(\frac{1 + f_R}{f_{RR}} - R \right). \tag{2.6}$$

The Compton wavelength of the field is then given by $\lambda_{f_R} \equiv m_{\text{eff}}^{-1}$.

It is very convenient to introduce a dimensionless quantity:

$$B = \frac{f_{RR}}{1 + f_R} R' \frac{H}{H'} \tag{2.7}$$

It has been shown [9] that in the high-curvature regime B is connected to the Compton wavelength via:

$$B^{1/2} \sim \lambda_{f_R} H \tag{2.8}$$

and thus is essentially the Compton wavelength of f_R at the background curvature in units of the horizon length.

In the static limit with $|f_R| \ll 1$ and $|f/R| \ll 1$, Eqn. 2.4 becomes

$$\bigtriangledown^2 f_R \approx \frac{1}{3}(R - \kappa^2 \rho) \tag{2.9}$$

where ρ is the local density. This equation has 2 modes of solutions. One is the very high curvature $R \approx \kappa^2 \rho$ and the other one is the low curvature (but still high compared to the background density) $R \ll \kappa^2 \rho$. For more on the interplay of these two regimes and applications in solar system observations see [9].

Let's now move on to the expansion history. For the model to yield behavior that is observationally viable requires a choice for the present day value of the f_R field $f_{R0} \ll 1$. This is equivalent to $R_0 \gg m^2$. In that case the approximation $R \gg m^2$ is valid for the whole expansion history and we have:

$$\lim_{m^2/R \to 0} f(R) \approx -\frac{c_1}{c_2} m^2 + \frac{c_1}{c_2^2} m^2 \left(\frac{m^2}{R} \right)^n \tag{2.10}$$

In the limiting case of $c_1/c_2^2 \to 0$ at fixed c_1/c_2 we obtain a cosmological constant behavior ΛCDM. Thus to approximate the ΛCDM expansion history with a cosmological constant Ω_Λ and matter density Ω_m we set:

$$\frac{c_1}{c_2} \approx 6 \frac{\Omega_\Lambda}{\Omega_m} \tag{2.11}$$

Fixing c_1/c_2 leaves 2 of the orignal 3 parameters of the model, expressed for example as n and c_1/c_2^2, to control how closely the model mimics ΛCDM. Larger n mimics until later in the expansion history, while smaller c_1/c_2^2 mimics it more closely.

For flat ΛCDM we have the following relations:

$$R \approx 3m^2 \left(a^{-3} + 4\frac{\Omega_\Lambda}{\Omega_m} \right) \tag{2.12}$$

$$f_R = -n\frac{c_1}{c_2^2} \left(\frac{m^2}{R} \right)^{n+1} \tag{2.13}$$

As we will see later these are the necessary ingredients for the application of perturbation theory to the model.

Finally we need to obtain a suitable parametrization of the mode. At the present epoch we have:

$$R_0 \approx m^2 \left(\frac{12}{\Omega_m} - 9 \right) \tag{2.14}$$

$$f_{R0} \approx -n\frac{c_1}{c_2^2} \left(\frac{12}{\Omega_m} - 9 \right)^{-n-1} \tag{2.15}$$

In particular, for $\Omega_\Lambda = 0.76$ and $\Omega_m = 0.24$, we have $R_0 = 41m^2$ and $f_{R0} \approx -n\ c_1/c_2^2/(41)^{n+1}$. ¿From now on we will parametrize the model through f_{R0} and n. Fig. 9 in [9] shows that there is a wide range of viable parameter values which satisfy Solar system and Galaxy requirements. We re-iterate that what makes this particular $f(R)$ model viable is its Chameleon behavior – the possibility of uniting galaxy and solar system observations with the expansion of the Universe.

2.3 Perturbation Formalism

By definition, the dark sector (dark matter and dark energy) can only be inferred from its gravitational consequences. In general relativity, gravity is determined by the total

stress-energy tensor of all matter and energy ($G_{\mu\nu} = 8\pi G\ T_{\mu\nu}$).

We may consider the Hubble parameter $H(z)$ to be fixed by observations. In a dark energy model, $\bar{\rho}$ is given by the Friedman equation of GR: $\bar{\rho} = 3H^2/8\pi G$. The equation of state parameter is $w = -1 - 2\dot{H}/3H^2$. The corresponding modified gravity model has matter density to be determined from its Friedman-like equation. We will consider MG models dominated by dark matter and baryons at late times.

2.3.1 Metric and fluid perturbations

With the smooth variables fixed, we will consider perturbations as a way of testing the models. In the Newtonian gauge, scalar perturbations to the metric are fully specified by two scalar potentials Ψ and Φ:

$$ds^2 = -(1 - 2\Psi)\ dt^2 + (1 - 2\Phi)\ a^2(t)\ d\vec{x}^2 \tag{2.16}$$

where $a(t)$ is the expansion scale factor. This form for the perturbed metric is fully general for any metric theory of gravity, aside from having excluded vector and tensor perturbations (see [34] and references therein for justifications). Note that Ψ corresponds to the Newtonian potential for the acceleration of particles, and that in general relativity $\Phi = -\Psi$ in the absence of anisotropic stresses.

A metric theory of gravity relates the two potentials above to the perturbed energy-momentum tensor. We introduce variables to characterize the density and velocity perturbations for a fluid, which we will use to describe matter and dark energy. The density fluctuation δ is given by

$$\delta(\vec{x}, t) \equiv \frac{\rho(\vec{x}, t) - \bar{\rho}(t)}{\bar{\rho}(t)} \tag{2.17}$$

where $\rho(\vec{x},t)$ is the density and $\bar{\rho}(t)$ is the cosmic mean density. The second fluid variable is the divergence of the peculiar velocity

$$\theta \equiv \nabla_j T_0^j/(\bar{p}+\bar{\rho}) = \vec{\nabla}\cdot\vec{v}, \tag{2.18}$$

where $\vec{v}$ is the (proper) peculiar velocity. Choosing θ instead of the vector $\mathbf{v}$ implies that we have assumed $\mathbf{v}$ to be irrotational. Our notation and formalism follows that of [10].

In principle, observations of large-scale structure can directly measure the four perturbed variables introduced above: the two scalar potentials Ψ and Φ, and the density and velocity perturbations specified by δ and θ. It is convenient to work with the Fourier transforms, such as:

$$\hat{\delta}(\vec{k},t) = \int d^3x\ \delta(\vec{x},t)\ e^{-i\vec{k}\cdot\vec{x}} \tag{2.19}$$

When we refer to length scale λ, it corresponds to a a statistic such as the power spectrum on wavenumber $k = 2\pi/\lambda$. We will henceforth work exclusively with the Fourier space quantities and drop the $\hat{}$ symbol for convenience.

2.3.2 Linearized fluid equations

We will use the perturbation theory equations for the quasi-static regime of the growth of perturbations. We begin with the fluid equations in the Newtonian gauge, following the formalism and notation of [35].

For minimally coupled gravity models with baryons and cold dark matter, but without dark energy, we can neglect pressure and anisotropic stress terms in the evolution equations to get the continuity equation:

$$\dot{\delta} = -\left(\frac{\theta}{a} - 3\dot{\Phi}\right) \simeq -\frac{\theta}{a}\ , \tag{2.20}$$

where the second equality follows from the quasi-static approximation as for GR. The Euler equation is:

$$\dot{\theta} = -H\theta - \frac{k^2\Psi}{a} \ . \tag{2.21}$$

We parametrize modifications in gravity by two functions $\tilde{G}_{\rm eff}(k,t)$ and $\eta(k,t)$ to get the analog of the Poisson equation and a second equation connecting Φ and Ψ [36, 10]. We first write the generalization of the Poisson equation in terms of an effective gravitational constant $G_{\rm eff}$:

$$k^2\Phi = -4\pi G_{\rm eff}(k,t)\bar{\rho}_{\rm MG}a^2\delta_{\rm MG} \ . \tag{2.22}$$

Note that the potential Φ in the Poisson equation comes from the spatial part of the metric, whereas it is the "Newtonian" potential Ψ that appears in the Euler equation (it is called the Newtonian potential as its gradient gives the acceleration of material particles). Thus in MG, one cannot directly use the Poisson equation to eliminate the potential in the Euler equation. A more useful version of the Poisson equation would relate the sum of the potentials, which determine lensing, with the mass density. We therefore introduce $\tilde{G}_{\rm eff}$ and write the constraint equations for MG as

$$k^2(\Phi - \Psi) = -8\pi\tilde{G}_{\rm eff}(k,t)\bar{\rho}_{\rm MG}a^2\delta_{\rm MG} \tag{2.23}$$

$$\Phi = -\Psi\ \eta(k,t) \tag{2.24}$$

where $\tilde{G}_{\rm eff} = G_{\rm eff}(1+\eta^{-1})/2$.

The parameter $\tilde{G}_{\rm eff}$ characterizes deviations in the $(\Phi-\Psi)$-δ relation from that in GR. Since the combination $\Phi - \Psi$ is directly responsible for gravitational lensing, $\tilde{G}_{\rm eff}$ has a specific physical meaning: it determines the power of matter inhomogeneities to

distort light. This is the reason we prefer it over working with more direct generalization of Newton's constant, $G_{\rm eff}$.

With the linearized equations above, the evolution of either the density or velocity perturbations can be described by a single second order differential equation. From Eqns. 2.20 and 2.21 we get, for the linear solution, $\delta(\vec{k},t) \simeq \delta_{initial}(\vec{k})D(k,t)$,

$$\ddot{\delta} + 2H\dot{\delta} + \frac{k^2\Psi}{a} = 0. \tag{2.25}$$

For a given theory, Eqns. 2.23 and 2.24 then allow us to substitute for Ψ in terms of δ to determine $D(k,t)$, the linear growth factor for the density:

$$\ddot{D} + 2H\dot{D} - \frac{8\pi\tilde{G}_{\rm eff}}{(1+\eta)}\bar{\rho}a^2\ D = 0. \tag{2.26}$$

What we need now are $\tilde{G}_{\rm eff}$ and η for our modified gravity model.

2.3.3 Parametrized post-Friedmann framework

Hu & Sawicki [9] also developed a formalism for simultaneous treatment of the super-horizon and quasi-static regime for modified gravity theories (in particular $f(R)$ and DGP) [37] (see also [38]. They begin by describing the different regimes individually and the requirements they impose on the structure of such models. Consequently they describe a linear theory parametrization of the super-horizon and the quasi-static regime and test it against explicit calculation. What is important for this paper is the proposed interpolation function for the metric ratio

$$g = \frac{\Phi + \Psi}{\Phi - \Psi} \tag{2.27}$$

For consistency we will express formulae from Hu & Sawicki in terms of physical time instead of expansion factor. We start with a background FRW universe for which we have the curvature in terms of the Hubble parameter $R = 6\dot{H} + 12H^2$. As we mentioned the background evolution H is chosen to match that of flat ΛCDM. We can then compute the Compton parameter B for our preferred model since we know what $f(R)$, R and H are:

$$B = \frac{f_{RR}}{1 + f_R} \dot{R} \frac{H}{\dot{H}} \tag{2.28}$$

The next step is to look at the super-horizon regime. In that case we know how to calculate the potentials Φ and Ψ. Their evolution is given by [25]:

$$\begin{gathered} \ddot{\Phi} + \left(1 - \frac{\ddot{H}}{H\dot{H}} + \frac{\dot{B}}{H(1-B)} + B\frac{\dot{H}}{H^2}\right) H\dot{\Phi} + \\ \left(2\frac{\dot{H}}{H^2} - \frac{\ddot{H}}{H\dot{H}} + \frac{\dot{B}}{H(1-B)}\right) H^2\Phi = 0, (k_H \to 0) \end{gathered} \tag{2.29}$$

$$\Psi = \frac{-\Phi - B\dot{\Phi}/H}{1 - B}, (k_H \to 0) \tag{2.30}$$

This allows us to compute $g_{SH} = g(t, k_H \to 0)$.

Furthermore in the case of subhorizon evolution where $k_H = k/a(t)H \gg 1$ we have $g_{QS} = -\frac{1}{3}$ [25].

According to [37] in the case of $f(R)$ theories we can use the following interpolation functions for the metric ratio:

$$g(t, k) = \frac{g_{SH} + g_{QS}(c_g k_H)^{n_g}}{1 + (c_g k_H)^{n_g}} \tag{2.31}$$

The evolution then is well described by [37] $c_g = 0.71B^{1/2}$ and $n_g = 2$ In terms of the post-Newtonian parameter: $\eta = -\Phi/\Psi$ we have $g = (\eta - 1)/(\eta + 1)$.

We still need one more ingredient, $\tilde{G}_{\rm eff}$, which is given by [37]

$$\tilde{G}_{\rm eff}(k,t) = \frac{G}{1+f_R} \tag{2.32}$$

We now have all the needed components to use in equation (2.26) for the growth factor of density perturbations. Calculations of the fractional change in the linear density power spectrum compared to GR have been done [9]. We show these in Fig. 2.1, using $\tilde{G}_{\rm eff}$ and η for the particular model we investigate. We have assumed the transfer function for the concordance $\Lambda-$CDM model consistent with the 5-year WMAP data [1].

We can also use the relations given above to obtain the linear growth factors for θ and the potentials from D. Note that in general the growth factors for the potentials have a different k dependence than D.

2.4 The Bispectrum in Perturbation Theory

2.4.1 Nonlinear fluid equations

The fluid equations in the Newtonian regime are given by the continuity, Euler and Poisson equations. Keeping the nonlinear terms that have been discarded in the study of linear perturbations above, the continuity equations gives:

$$\dot{\delta} + \theta = -\int \frac{d^3k_1}{(2\pi)^3} \frac{\vec{k}\cdot\vec{k}_1}{k_1^2} \theta(\vec{k_1})\delta(\vec{k}-\vec{k}_1) \tag{2.33}$$

where the term on the right shows the nonlinear coupling of modes. Note that the time derivatives are with respect to conformal time in this section.

The Euler equation is

$$\dot{\theta} + H\theta + k^2\Psi = -\int \frac{d^3k_1}{(2\pi)^3} \frac{k^2\vec{k}_1\cdot(\vec{k}-\vec{k}_1)}{2k_1^2|\vec{k}_1-\vec{k}_2|^2} \theta(\vec{k_1})\theta(\vec{k}-\vec{k}_1) \tag{2.34}$$

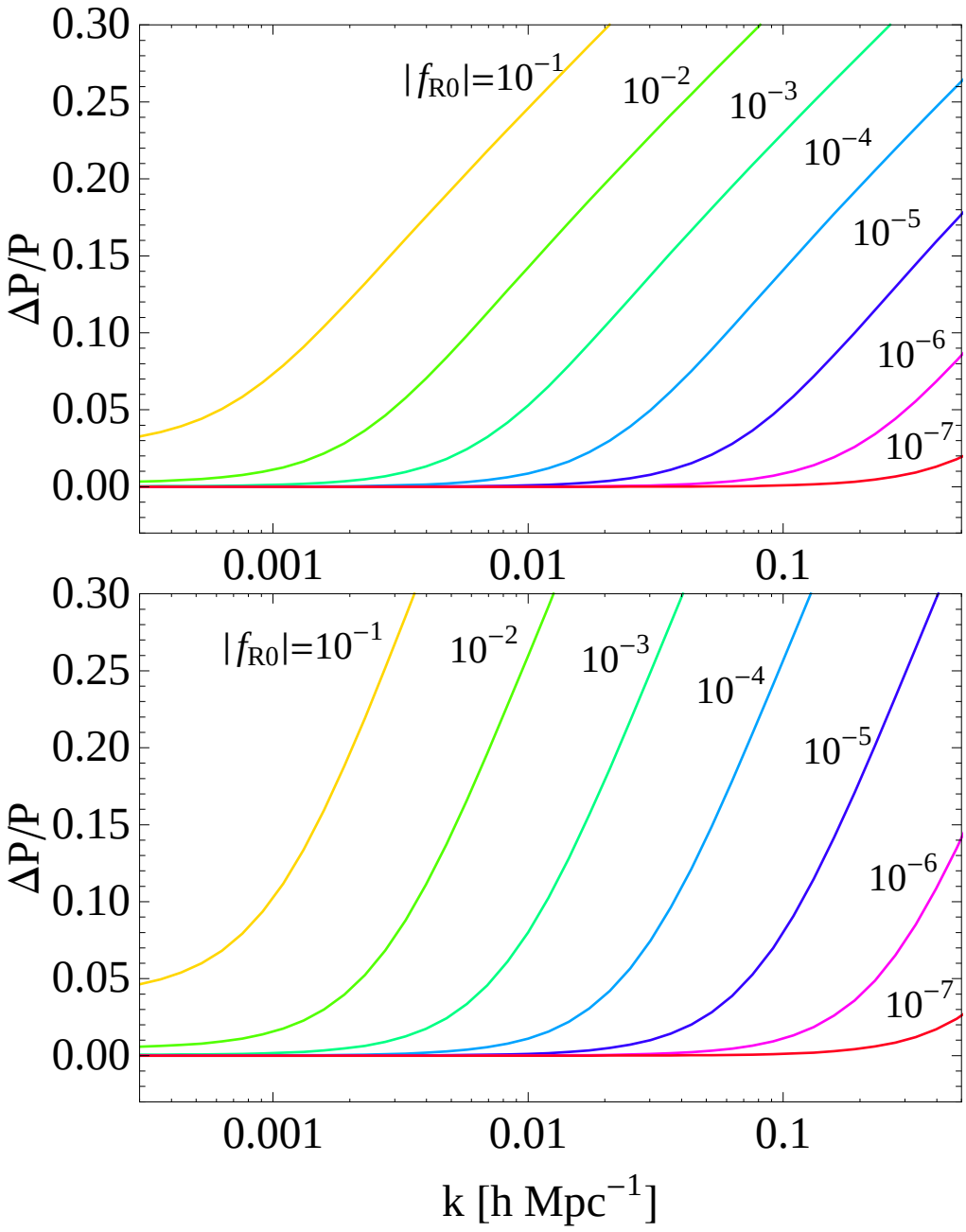

Figure 2.1: (Color online) Fractional change at $z = 0$ in the density power spectrum of the $f(R)$ model compared to ΛCDM for a set of choices of f_{R0}. The upper panel is the $n = 4$ model, while the lower panel has $n = 1$. This figure can be compared with Fig. 4 in [9].

We neglect pressure and anisotropic stress as the energy density is taken to be dominated by non-relativistic matter [39]. The Poisson equation is given by Eqn. 2.23 and supplemented by the relation between Ψ and Φ given by Eqn. 2.24. Using these equations we can substitute for Ψ in the Euler equation to get

$$\begin{aligned} \dot{\theta} \quad &+ \quad H\theta + \frac{8\pi\tilde{G}_{\rm eff}}{(1+\eta)}\bar{\rho}_{\rm MG}a^2\delta \\ &= \quad -\int \frac{d^3k_1}{(2\pi)^3}\frac{k^2\vec{k}_1\cdot(\vec{k}-\vec{k}_1)}{2k_1^2|\vec{k}_1-\vec{k}_2|^2}\theta(\vec{k_1})\theta(\vec{k}-\vec{k}_1) \end{aligned} \tag{2.35}$$

Eqns. 2.33 and 2.35 are two equations for the two variables δ and θ. They constitute a fully nonlinear description and can be solved once η and $\tilde{G}_{\rm eff}$ are specified. An important caveat is that they may nevertheless be invalid on strongly nonlinear scales or for particular MG theories. For the $f(R)$ model considered here, they are valid on scales well above 1 Mpc; on smaller scales the chameleon mechanism modifies the growth of structure [40]. Since we will use perturbation theory, our approach breaks down once $\delta \sim 1$ in any case.

Next we consider perturbative expansions for the density field and the resulting behavior of the power spectrum and bispectrum. Let $\delta = \delta_1 + \delta_2 + ...$ where $\delta_2 \sim O(\delta_1^2)$. In the quasilinear regime, i.e. on length scales between ∼10-100 Mpc, mode coupling effects can be calculated using perturbation theory. While this is strictly true only for general relativity, a MG theory that is close enough to GR to fit observations can also be expected to have this feature.

For MG, following [10], let us simplify the notation by introducing the function:

$$\zeta(k,t) = \frac{8\pi\tilde{G}_{\rm eff}}{(1+\eta)}, \tag{2.36}$$

which is simply $4\pi G$ in GR but can vary with time and scale in MG theories. The evolution of the linear growth factor is given by substituting for Ψ in Eqn. 2.37 to get (as above,

but with conformal time here)

$$\ddot{\delta_1} + H\dot{\delta_1} - \zeta\bar{\rho}a^2\delta_1 = 0. \tag{2.37}$$

The linear growth factor has a scale dependence for our $f(R)$ as shown in Fig. 1.

In addition we show below that the second order solution has a functional dependence on $\tilde{G}_{\rm eff}$ and η that can differ from GR. Thus potentially distinct signatures of the scale and time dependence of $\tilde{G}_{\rm eff}(k,z)$ can be inferred from higher order terms. These rely either on features in k and t in measurements of $P_{\Phi-\Psi}$ and P_δ, or on the three-point functions which can have distinct signatures of MG even at a single redshift [41]. Quasi-linear signatures due to $\eta(k,z)$ can also be detected via second order terms in the redshift distortion relations for the power spectrum and bispectrum. Our discussion generalizes that of [18] who examined a Yukawa-like modification of the Newtonian potential.

2.4.2 Second order solution

From a perturbative treatment of Eqns. 2.33 and 2.35 the second order term for the growth of the density field is given by [10]

$$\ddot{\delta_2} + H\dot{\delta_2} - \bar{\rho}a^2\zeta\delta_2 =$$

$$HI_1[\dot{\delta_1},\delta_1] + I_2[\dot{\delta_1},\dot{\delta_1}] + \dot{I}_1[\dot{\delta_1},\delta_1], \tag{2.38}$$

where I_1 and I_2 denote convolution like integrals of the two arguments shown, given by the right-hand side of equations 2.33 and 2.35 as follows

$$I_1[\dot{\delta_1},\delta_1](\vec{k}) = \int \frac{d^3k_1}{(2\pi)^3}\frac{\vec{k}\cdot\vec{k}_1}{k_1^2}\dot{\delta}_1(\vec{k_1})\delta_1(\vec{k}-\vec{k}_1) \tag{2.39}$$

and

$$I_2[\dot{\delta_1},\dot{\delta_1}](\vec{k}) = \int \frac{d^3k_1}{(2\pi)^3}\frac{k^2\vec{k}_1\cdot(\vec{k}-\vec{k}_1)}{2k_1^2|\vec{k}_1-\vec{k}_2|^2}\dot{\delta}_1(\vec{k_1})\dot{\delta}_1(\vec{k}-\vec{k}_1). \tag{2.40}$$

Finally, the last term in Eqn. 2.38 is simply $\dot{I}_1[\dot{\delta}_1, \delta_1] = I_1[\ddot{\delta}_1, \delta_1] + I_1[\dot{\delta}_1, \dot{\delta}_1]$. Note that by continuing the iteration, higher order solutions can be obtained.

2.4.3 Three-point correlations

Distinct quasilinear effects are found in three-point correlations – we will use the Fourier space bispectrum. Recently Tatekawa & Tsujikawa have performed a similar perturbative analysis and presented results on the skewness [43]. We prefer to use the bispectrum as it allows one to study specific quasilinear signatures contained in the configuration dependence of triangle shapes. The bispectrum for the density field B_δ is defined by

$$\langle \delta(\vec{k}_1)\delta(\vec{k}_2)\delta(\vec{k}_3)\rangle = (2\pi)^3 \delta_{\rm D}(\vec{k}_1 + \vec{k}_2 + \vec{k}_3) B_\delta(\vec{k}_1, \vec{k}_2, \vec{k}_3) \tag{2.41}$$

Since $B_\delta \sim \langle \delta^3 \rangle \sim \langle \delta_1^2 \delta_2 \rangle$ (using $\langle \delta_1^3 \rangle = 0$ for an initially Gaussian density field) at tree level, the second order solution enters at leading order in the bispectrum. Note also that the wavevector arguments of the bispectrum form a triangle due to the Dirac delta function on the right-hand side above.

The bispectrum is the lowest order probe of gravitationally induced non-Gaussianity. A useful version of it is the reduced bispectrum Q, which for the density field δ is given by

$$Q_\delta \equiv \frac{B_\delta(\vec{k}_1, \vec{k}_2, \vec{k}_3)}{P_\delta(k_1)P_\delta(k_2) + P_\delta(k_2)P_\delta(k_3) + P_\delta(k_1)P_\delta(k_3)}. \tag{2.42}$$

Q is useful because it is insensitive to the amplitude of the power spectrum; thus e.g. at tree level and in the case of a scale free linear power spectrum $P(k) \sim k^n$ it is static and scale independent for regular gravity [42].

2.5 Results

In Fig. 2.2 we present the bispectrum for the $f(R)$ model and its dependence on scale for two different redshifts. For comparison we also show the bispectra predicted in GR. In the lower panel we present the ratio of the $f(R)$ bispectra to that in GR. We have assumed the transfer function for the concordance $\Lambda-$CDM model consistent with the 5-year WMAP data [1]. Calculation is done at tree level with $\Omega_m = 0.24$. The bispectra in $f(R)$ gravity are enhanced relative to GR, increasingly so at high-k. The enhancement is of order 10-20% for observationally relevant scales around $k \sim 0.1$ and redshifts below unity.

We turn our attention to the reduced bispectrum Q, which is expected to show features not associated with the linear power spectrum [42]. We show two relevant cases. The first one is with equilateral triangles, shown in Fig. 2.3. Deviations from GR are at the percent-level, which makes them impossible to detect with current measurements. Qualitatively, the parameters of the model do influence the scale and time dependence of the reduced bispectrum.

Slightly stronger deviations from regular gravity are observed for isosceles triangle configurations, shown in Fig. 2.4. Once again strong scale and time variation is observed when changing the model parameters. We also show the angular dependence of the reduced bispectrum for 3:1 ratio configurations and its comparison to regular gravity in Fig. 2.5.

2.5.1 Does the Linear Growth Factor Determine Nonlinear Clustering?

Quasilinear effects, and the bispectrum in particular, show signatures of gravitational clustering. However, we find that the reduced bispectrum Q remains very close

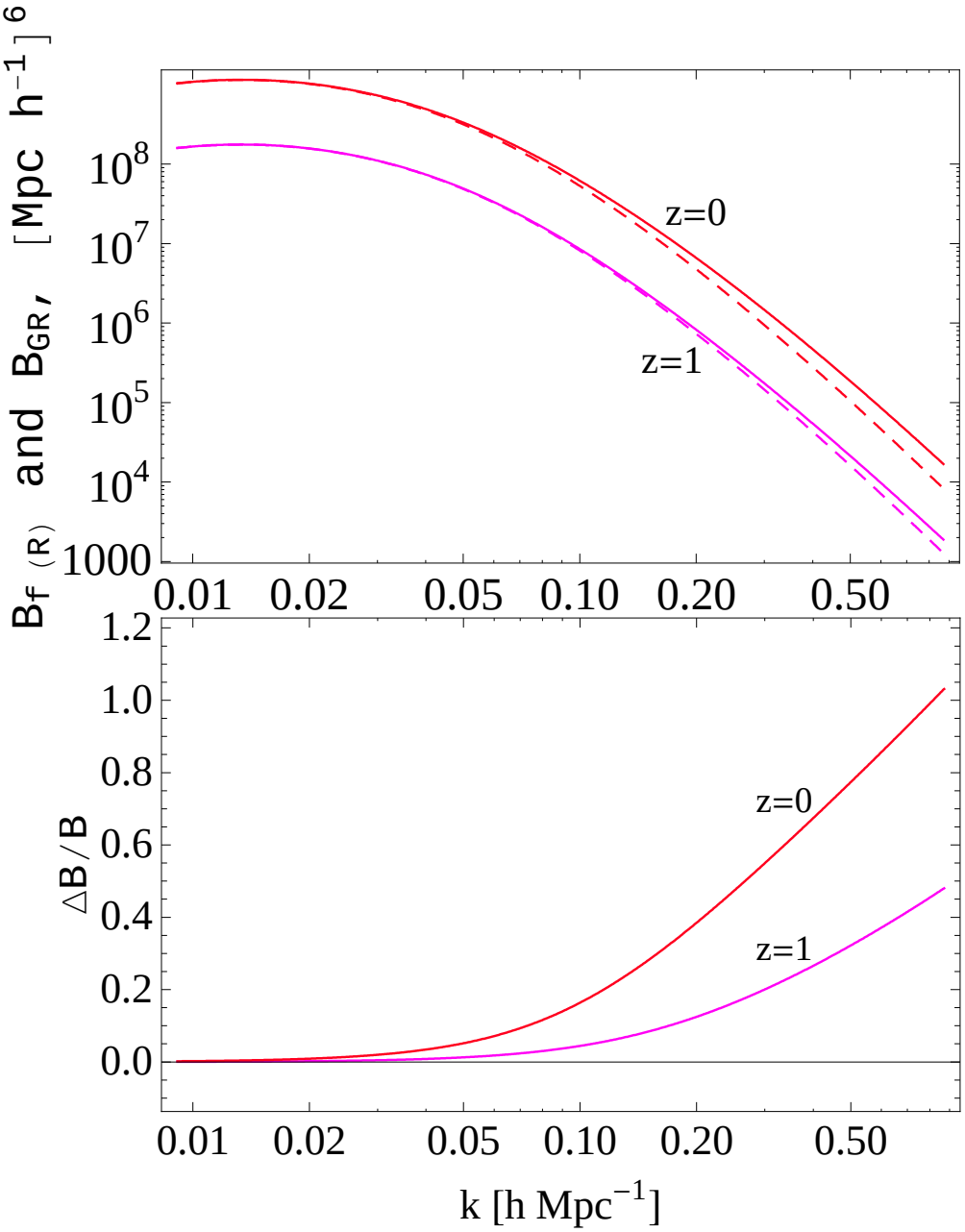

Figure 2.2: (Color online) *Upper panel:* The Bispectrum of the $f(R)$ model for equilateral triangles depending on scale for the $f(R)$ model with $f_{R0} = 10^{-5}$, $n = 1$. The corresponding regular gravity bispectrum is shown as the dashed curve. *Lower panel:* The Ratio of the f(R) Bispectrum to the regular gravity one.

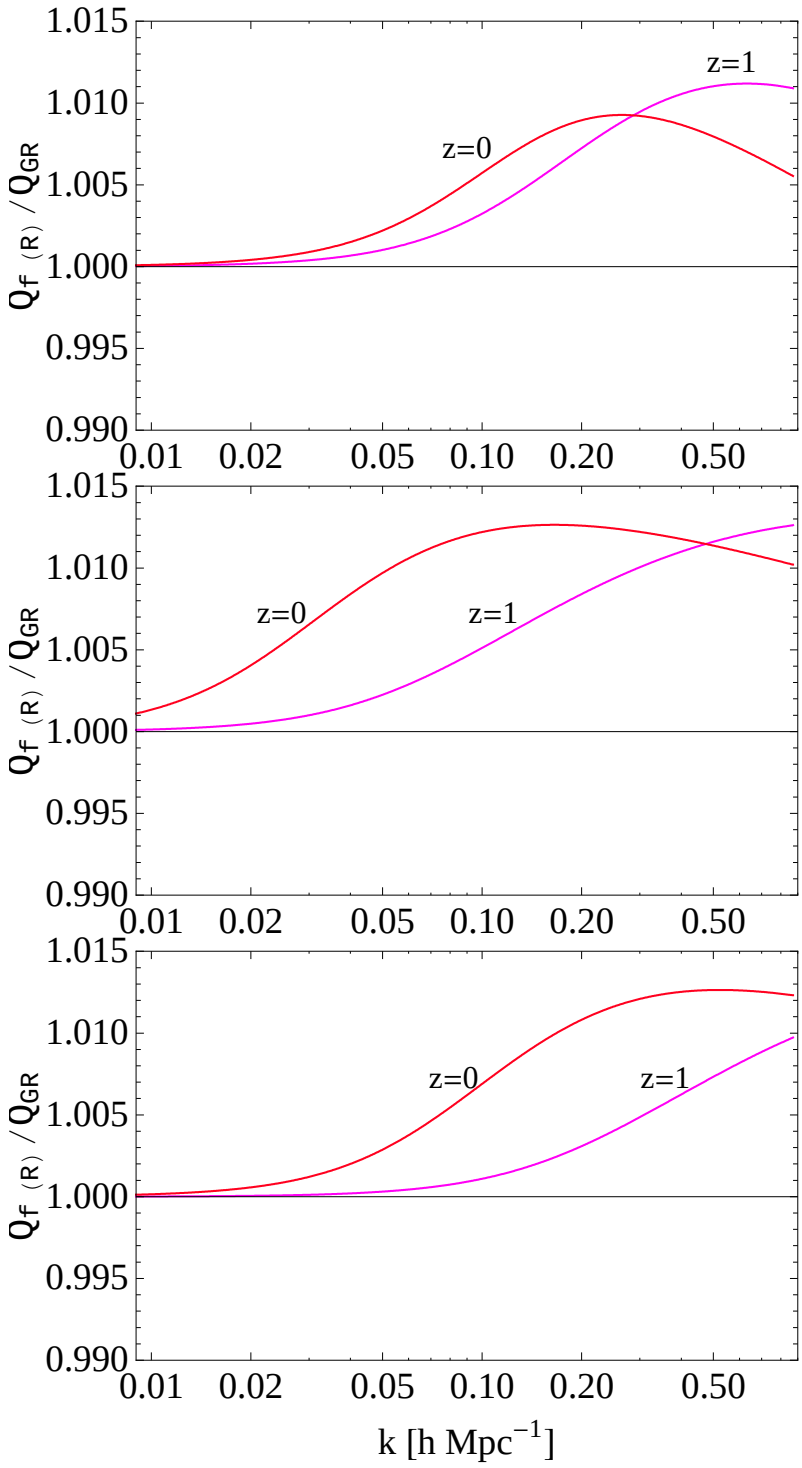

Figure 2.3: (Color online) The reduced bispectrum Q for equilateral triangles for the $f(R)$ model compared to regular gravity. *Top panel:* $f_{R0} = 10^{-5}$, $n = 1$. *Middle panel:* $f_{R0} = 10^{-4}$, $n = 4$. *Bottom panel:* $f_{R0} = 10^{-5}$, $n = 4$.

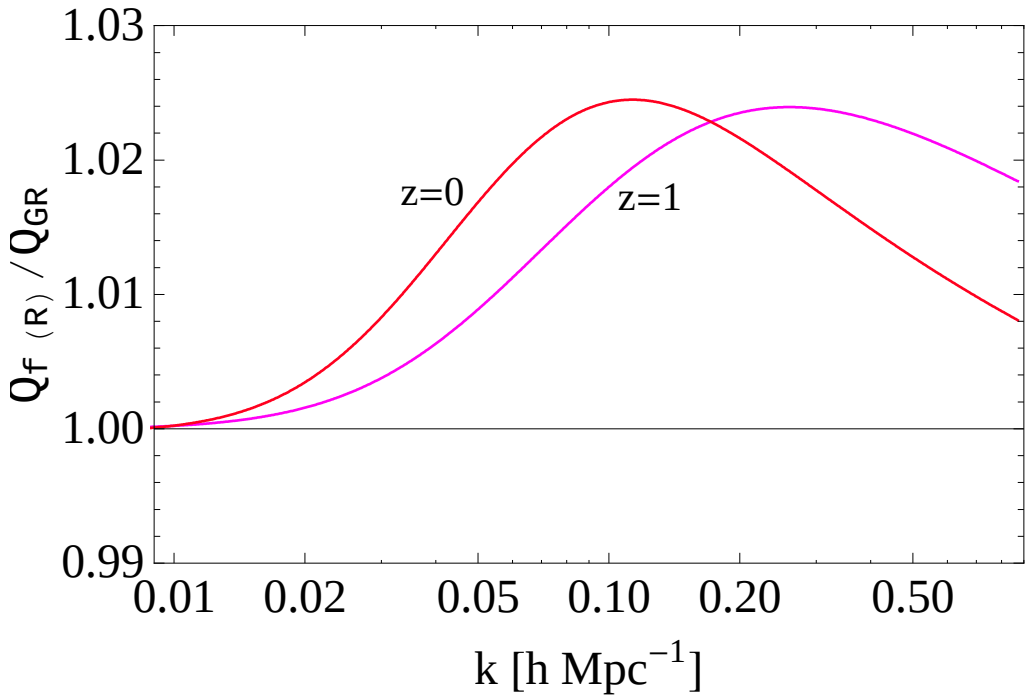

Figure 2.4: (Color online) The reduced bispectrum Q for isosceles triangles (ratio of sides lengths 1:3:3), where the x-axis shows the length of the smallest k in the triangle. The ratio of Q for the $f(R)$ model with $f_{R0} = 10^{-5}$, $n = 1$ to regular gravity is shown.

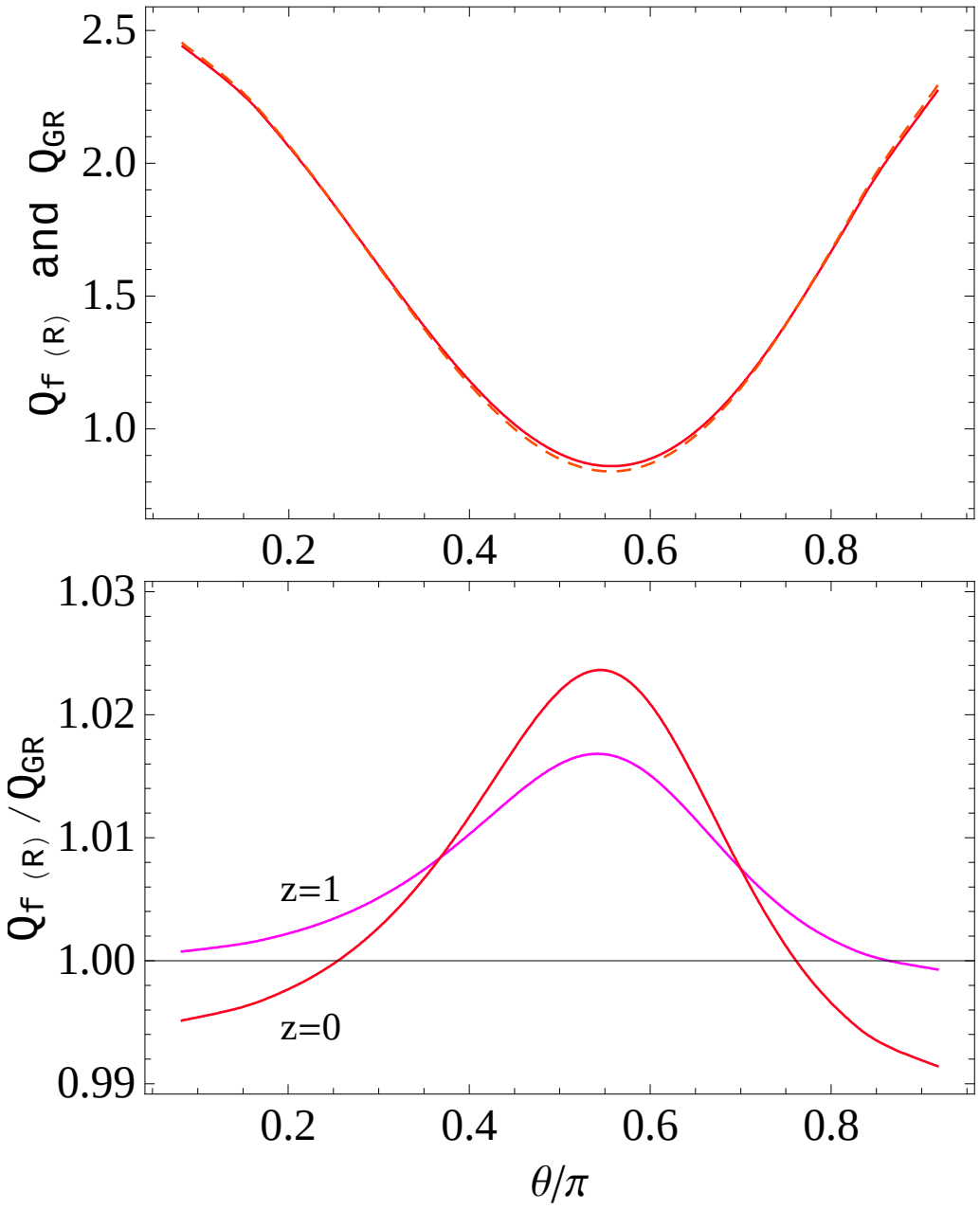

Figure 2.5: (Color online) *Upper panel:* The angular dependence of the reduced bispectrum Q for triangles with the two fixed side lengths in the ratio 1:3 and $k = 0.1h$/Mpc for the smaller one. The $f(R)$ model with $f_{R0} = 10^{-5}$, $n = 1$ at $z = 0$ is used. The dashed line shows the prediction for GR. *Lower panel:* Comparison to regular gravity at two redshifts. We can observe that for obtuse shapes ($\theta \sim 0$) our model predicts a lower Q for $f(R)$ gravity, while for shapes close to isosceles it is enhanced.

to to that of GR in the modified gravity models we have considered (see also [43] for a related study). This is qualitatively similar to previous findings about the insensitivity of Q to cosmological parameters within a GR context [42].

Thus the deviations in the bispectrum are largely determined by the linear growth factor. Ambitious future surveys will be needed to achieve the percent level measurements required to probe the unique signatures of modified gravity in the bispectrum. On the other hand, this means that the bispectrum can be used as a consistency check on the power spectrum. It has been shown that the bispectrum contains information comparable to the power spectrum, thus improving the signal-to-noise [44] . Equally importantly, it is affected by sources of systematic error in different ways and contains signatures of gravitational clustering that are unlikely to be mimicked by other effects.

Currently the results of N-body simulations for this f(R) model [40] show that our assumptions are consistent with their result for the power spectrum on scales $k \lesssim 0.2[h/Mpc]$). On smaller scales, the onset of nonlinearity and the chameleon mechanism invalidate our results. The deviation from the linear prediction grows fast and is of order 10% on scales $k \sim 0.2 - 0.5[h/Mpc]$ depending on the model. So the results in our plots on those scales will need to be carefully checked with simulations.

Modifications to the Newtonian potential were simulated by [32] (also see [18],[45]). These simulation studies found that, to a good approximation, the nonlinear power spectra depend only on the initial conditions and linear growth. The standard fitting formulae for Newtonian gravity [46] were adapted to predict the nonlinear spectrum at a given redshift. Therefore tests for modified gravity using the power spectrum require either a measurement of the scale dependent growth factor (in combination with the initial spec-

trum measured from the CMB), or of measurements at multiple epochs. More likely a combination of probes will be used for robust tests of gravity (see e.g. [10]).

Related studies of nonlinear clustering in $f(R)$ models or DGP gravity are in progress [11, 48, 47]; these authors are considering the power spectra, bispectra as well as halo properties, in particular the halo mass function. The $f(R)$ studies of [40] and [11] show distinct effects of the chameleon field on small scales (comparable to galaxy and cluster sized halos for most models); [37] suggest a fit for the nonlinear power spectrum with additional parameters that describe the transition to the small-scale regime. The DGP study of [47] requires inclusion of nonlinear terms in the Poisson equation. So clearly for different models there can be new nonlinearities and couplings to additional fields that impact the small-scale regime of clustering. Even so, for a class of models that includes the $f(R)$ models studied here, the quasistatic, Newtonian description parameterized by $\tilde{G}_{\rm eff}$ and $\eta = \Phi/\Psi$ applies over a wide range of scales relevant for large-scale structure observations. In this regime, to a good approximation, many clustering statistics can be predicted using the linear growth factor and the standard gravity formalism.

2.5.2 Implications for Lensing and Dynamics

Lensing observations provide estimates of the convergence power spectrum and bispectrum (see e.g. [49]). For a rough estimate of these quantities, we take the source galaxies distribution to be a delta function at a given redshift and take the lensing matter to be situated at half the distance. Since we have taken the expansion history to be ΛCDM, so comoving distances are the same as in GR. With these approximations, $P_\kappa \propto P_{\Phi-\Psi}$. From Eqn. 2.23 we can see that the difference of the lensing behavior of our modified

gravity case and the regular gravity one is given by (see also [41])

$$P_{\Phi-\Psi} \propto P_\delta \left(\frac{\tilde{G}_{\rm eff}(k, t_{1/2})}{G} \right)^2 \tag{2.43}$$

where $t_{1/2}$ is the physical time at the redshift of the lensing matter.

Thus we can write:

$$\frac{P_{\kappa MG}}{P_{\kappa GR}} \propto \frac{P_{\delta MG}}{P_{\delta GR}} \left(\frac{\tilde{G}_{\rm eff}(k, t_{1/2})}{G} \right)^2 \tag{2.44}$$

Analogously we can see that the ratio of convergence bispectra behaves like $(\tilde{G}_{\rm eff}(k, t_{1/2})/G)^3$ but the ratio of the reduced bispectra behaves like

$$\frac{Q_{\kappa MG}}{Q_{\kappa GR}} \propto \frac{Q_{\delta MG}}{Q_{\delta GR}} \frac{G}{\tilde{G}_{\rm eff}(k, t_{1/2})} \tag{2.45}$$

Thus the convergence power spectrum and reduced bispectrum could be successfully used to differentiate and/or rule out models of modified gravity. Unfortunately in the currently discussed model we have Eqn. 2.32:

$$\tau(k, t(a)) = \frac{\tilde{G}_{\rm eff}}{G} = \frac{1}{1 + f_R(a)} \tag{2.46}$$

which deviates from unity at the order of f_{R0}, which is much smaller than unity. Thus the convergence power spectrum and reduced bispectrum follow almost identically the predictions for their matter counterparts. This means that the comparison of lensing to tracers of mass fluctuations does not reveal distinct signatures of $f(R)$ gravity.

The Newtonian potential Ψ drives dynamical observables such as the redshift space power spectrum of galaxies [10], [36]. The velocity growth factor D_θ is related to the density growth factor via the function β:

$$D_\theta \propto a\beta HD \tag{2.47}$$

where $\beta = d\ln D/d\ln a$. This function varies with scale and expansion factor for our $f(R)$ models. Both τ and β can be seen in Fig. 2.6 which clearly shows that observables based on peculiar velocities would show a clear signature of $f(R)$ gravity. More detailed calculations of lensing and velocity statistics are beyond the scope of this study.

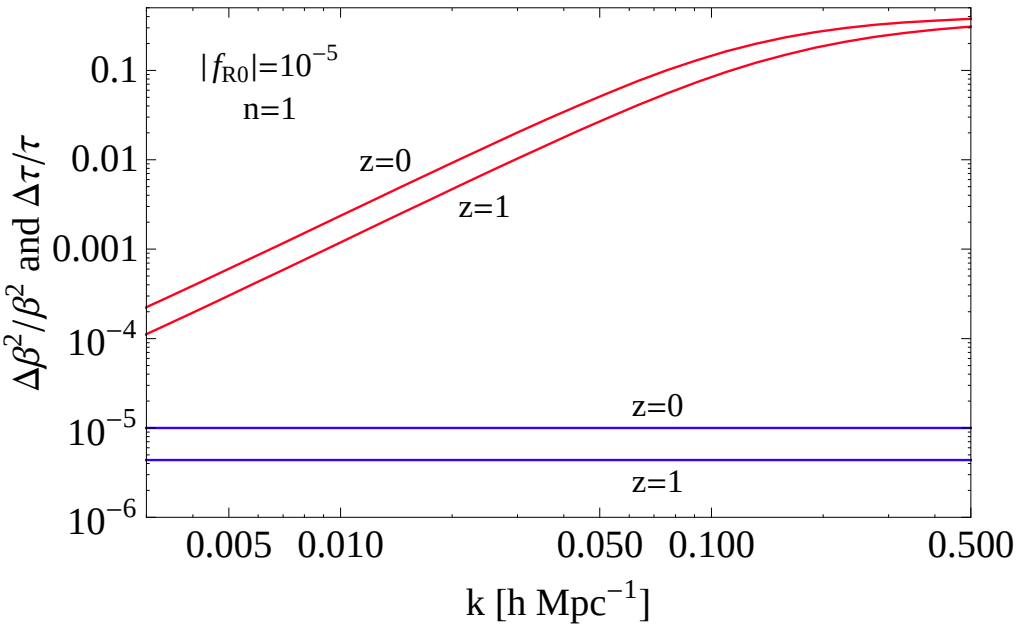

Figure 2.6: (Color online) The fractional change in τ (blue lines) and β^2 (red lines) for the $f(R)$ model with $f_{R0} = 10^{-5}$, $n = 1$ compared to GR as a function of scale.

2.6 Discussion

In this paper we studied the growth of structure in an $f(R)$ modified gravity model [9]. In the quasilinear regime, we used perturbation theory to calculate the three-point correlation function, the bispectrum, of matter. Our results are applicable up to scales at which the derivation of the quasi-linear perturbation theory is still valid.

We found that in the bispectrum the dominant behavior is due to the difference

in the linear growth factors between the modified gravity model and regular gravity. The bispectrum itself shows significant departures in scale and time compared to the predictions of GR. However the reduced bispectrum, which is independent of the linear growth factor in perturbation theory for GR, remains within a few percent of the regular gravity prediction. It does show interesting signatures of modified gravity at the percent level.

Our results are consistent with studies of the nonlinear regime via N-body simulations, which have found that on a wide range of scales the nonlinear power spectrum can be predicted using the (modified gravity) linear growth factor in the standard formulae developed for Newtonian gravity. Our results imply that three-point correlations follow this trend at the few percent level. (The regime around and inside halos probed by [40] to test the chameleon behavior is not included in our perturbative study.) It would be interesting to compare perturbative and simulation results for the bispectrum for the models considered here and other modified gravity models.

Upcoming surveys in the next five years will not attain the percent level accuracy at which the reduced bispectrum shows distinct signatures of $f(R)$ gravity. In this timeframe, the bispectrum will be useful as a consistency check on potential deviations from GR found in the power spectrum. Such a check is useful since measurement errors and scale dependent biases of tracers can mimic some of the deviations in the power spectrum. Next generation surveys, to be carried out in the coming decade, will provide sufficient accuracy to test the distinct signatures seen in our results for the reduced bispectrum. With these surveys, the bispectrum can provide truly new signatures of gravity.

Acknowledgments: We are grateful to Jacek Guzik, Wayne Hu, Mike Jarvis, Justin Khoury, Matt Martino, Fabian Schmidt, Roman Scoccimarro, Ravi Sheth, Fritz

Stabenau, Masahiro Takada and Pengjie Zhang. BJ is supported in part by NSF grant AST-0607667.

Chapter 3

Simulating spherical collapse

3.1 Introduction

Recently the nonlinear regime of structure formation in $f(R)$ modified gravity theories has been actively studied, focusing on the effects of the chameleon field which alters the dynamics of mass clustering. A series of papers [9, 11, 12, 37, 40] have explored the consequences of this evolution through simulations and comparison to analytical predictions. The evolution of isolated spherical overdensities in an expanding universe provides a useful approximation for structure in the Universe. In part using this model, [11] explores the topic of properties of dark matter halos that form galaxies and galaxy clusters. These in turn are an important tool for studying the nature of Cold Dark Matter and Dark Energy [10]. In [11] halo mass functions, linear bias and density profiles have been calculated to observe their differences from the Standard Model of cosmology - the ΛCDM model. In addition analytical calculations have been done in the two limiting cases of the $f(R)$ model:

1. The strong field regime, where $f(R)$ behaves like a ΛCDM model, but with a larger Newton's constant (by a factor of 4/3).

2. The weak field regime, where there is no observable difference from the Standard Model.

The results from these bounding situations have been compared to simulations by [11] and the observed differences have been discussed. Since the strength of gravity has been inside these two limiting cases, a reasonable expectation is that the final observed quantities should also remain inside the predictions. In this chapter we will explore the validity of such linear assumption by performing a direct simulation of a spherical collapse of an isotropic object. As chameleon $f(R)$ theories exhibit highly no-linear behavior and there exist coupled fields, it is worth checking through explicit calculation the naive expectation based on limiting cases. We want to be able to compare relevant quantities, like like δ_c, with the results from the analytical calculation in [11].

The evolution and collapse of spherical overdensities have been useful for modelling the formation of galaxy and cluster halos. In the Standard Model of gravity the problem can be approached analytically and we will outline the derivation presented in [11]. We start with the nonlinear and Euler equation for a non-relativistic pressureless fluid in comoving coordinates:

$$\begin{aligned} \frac{\partial \delta}{\partial t} + \frac{1}{a}\nabla \cdot (1+\delta)\mathbf{v} &= 0 \\ \frac{\partial \mathbf{v}}{\partial t} + \frac{1}{a}(\mathbf{v}\cdot\nabla)\mathbf{v} + H\mathbf{v} &= -\frac{1}{a}\nabla\Psi, \end{aligned} \tag{3.1}$$

where these equations continue to be valid for modifications of gravity that remain a metric theory [50]. These can now be joined together to form a second order equation for

δ.

$$\frac{\partial^2\delta}{\partial t^2} + 2H\frac{\partial\delta}{\partial t} - \frac{1}{a^2}\frac{\partial^2(1+\delta)v^iv^j}{\partial x^i\partial x^j} = \frac{\nabla\cdot(1+\delta)\nabla\Psi}{a^2} \tag{3.2}$$

This equation needs information about the velocity and potential fields. In the case of spherical top-hat distribution the velocity field takes the form $\mathbf{v} = A(t)\mathbf{r}$ to have a spatially constant divergence. Its amplitude is related to the top-hat density perturbation through the continuity equation:

$$\dot{\delta} + \frac{3}{a}(1+\delta)A = 0 \tag{3.3}$$

This leads to:

$$\frac{\partial^2 v^iv^j}{\partial x^i\partial x^j} = 12A^2 = \frac{4}{3}a^2\frac{\dot{\delta}^2}{(1+\delta)^2}, \tag{3.4}$$

and in the approximation of top-hat the equation for the evolution of δ becomes:

$$\frac{\partial^2\delta}{\partial t^2} + 2H\frac{\partial\delta}{\partial t} - \frac{4}{3}\frac{\dot{\delta}^2}{(1+\delta)} = \frac{(1+\delta)}{a^2}\nabla^2\Psi, \tag{3.5}$$

which is completed by the Poisson's equation for the potential:

$$\nabla^2\Psi = 4\pi G a^2\delta\rho_m. \tag{3.6}$$

It is common to express spherical collapse through the evolution of the radius of the top-hat. For that we use mass conservation:

$$M = \frac{4\pi}{3}r^3\bar{\rho}_m(1+\delta) = \text{const.} \tag{3.7}$$

to obtain the following relation:

$$\frac{\ddot{r}}{r} = H^2 + \dot{H} - \frac{\nabla^2\Psi}{3a^2} \tag{3.8}$$

Expressing derivatives in terms of scale factor $' = d/d\ln a$, with the useful substitution $y = \frac{r}{r_i} - \frac{a}{a_i}$, and using Poisson's equation we obtain:

$$y'' + \frac{H'}{H}y' = -\frac{1}{2}\frac{\Omega_m a^{-3} - 2\Omega_\Lambda}{\Omega_m a^{-3} + \Omega_\Lambda}y - \frac{1}{2}\frac{\Omega_m a^{-3}}{\Omega_m a^{-3} + \Omega_\Lambda}(\frac{a}{a_i} + y)\Delta, \tag{3.9}$$

where

$$\Delta = \left(\frac{1}{1 + ya_i/a}\right)^3 (1 + \delta_i) - 1. \tag{3.10}$$

In these coordinates collapse occurs when $y = -\frac{a}{a_i}$. The task of computing δ_c now reduces to the following: for a given a_i find an initial overdensity δ_i such that the collapse occurs at $a = 1$. Then using the linear growth factor in ΛCDM (see for example [50]) we extrapolate δ_i to the present epoch to obtain δ_c.

In the case of modified gravity analytical approach can not be used in the general case. Thus we need to use simulations. As described in [12] for simulations in the case of the particular $f(R)$ model we have chosen, the solution for the potential driving the dynamics of the evolution is coupled with the solution for the scalar field f_R [9]. In our case we deal with isotropic objects and thus have a one-dimensional system. In the first section we derive the radial equation for the f_R field. In subsequent sections we will describe the relaxations scheme for numerically solving the aforementioned equation, the dynamics code tests. After that we will focus on particular technical difficulties we encountered in performing the simulations and our approach in resolving them. Finally, we will outline the current results and the future work to be done.

3.2 Derivation of the radial equation for an isotropic object

Following [12] which set up the 3D simulation framework for the $f(R)$ chameleon model we start with:

$$\nabla^2 f_R = \frac{1}{3c^2}\left[\delta R(f_R) - 8\pi G\delta\rho\right] \tag{3.11}$$

$$\nabla^2\phi = \frac{16\pi G\rho_0}{3}\delta\rho - \frac{1}{6}\delta R(f_R). \tag{3.12}$$

For the purposes of numerical calculations we need to define relevant unitless quantities, and we find working in comoving coordinates more intuitive. Thus we adopt the usual definition of code units [12, 52, 53]:

$$\tilde{r} = \frac{x}{r_0 a}, \quad \tilde{t} = tH_0, \quad \tilde{\rho} = a^3 \frac{\rho}{\rho_0}, \tag{3.13}$$
$$\tilde{R} = a^3 \frac{R}{R_0}, \quad \tilde{c} = \frac{c}{r_0 H_0}, \quad \tilde{\phi} = \frac{\phi}{\phi_0}, \quad \tilde{p} = a\frac{v}{v_0},$$

where

$$\rho_0 = \rho_{c,0}\Omega_{M,0}, \quad R_0 = \frac{8\pi G\rho_0}{3}, \quad \phi_0 = (r_0 H_0)^2, \quad v_0 = r_0 H_0 \tag{3.14}$$

and r_0 is an appropriate length scale (used for example to define the size of the overdensity). Bare symbols X are physical coordinates/quantities while symbols with tilde $\tilde{X}$ are code quantities, symbols with bars $\bar{X}$ are average physical and symbols with both bar and tilde $\bar{\tilde{X}}$ are average code quantities.

Equations (3.11 3.12) then become the following in code units (Eqns. 25,27 in [12]):

$$\tilde{\nabla}^2 \delta f_R = \frac{\Omega_{M,0}}{a\tilde{c}^2}\left[\frac{\delta\tilde{R}}{3} - \delta\right] \tag{3.15}$$

$$\tilde{\nabla}^2 \tilde{\phi} = \frac{\Omega_{M,0}}{a}\left[-\frac{\delta\tilde{R}}{6} + 2\delta\right] \tag{3.16}$$

where

$$\delta = \frac{\rho - \bar{\rho}}{\bar{\rho}} = \tilde{\delta}. \tag{3.17}$$

The next step is to express $\delta\tilde{R}$ in terms of f_R in code coordinates. We start with (Eqn 9 in [12]):

$$\bar{R} = 8\pi G\bar{\rho}_M\left(\frac{1}{a^3} + 4\frac{\Omega_{\Lambda,0}}{\Omega_{M,0}}\right) \tag{3.18}$$

This is the average curvature in the $f(R)$ model. Thus:

$$\frac{\bar{R}}{R_0} = 3\frac{\bar{\rho}_M}{\rho_0}\left(\frac{1}{a^3} + 4\frac{\Omega_{\Lambda,0}}{\Omega_{M,0}}\right) \tag{3.19}$$

We arrive at:

$$\frac{\bar{R}}{R_0} = 3\left(\frac{1}{a^3} + 4\frac{\Omega_{\Lambda,0}}{\Omega_{M,0}}\right) \tag{3.20}$$

From that we also have:

$$\frac{\bar{R}(a=1)}{R_0} = 3\left(1 + 4\frac{\Omega_{\Lambda,0}}{\Omega_{M,0}}\right) \tag{3.21}$$

We also need the relation between f_R and R. Using (Eqn. 12 in [12]) defining $\bar{f}_R(a = 1) = f_{R0}$ and working in the case $n = 1$ we see that:

$$\frac{f_R}{f_{R0}} = \left(\frac{\bar{R}(a=1)}{R}\right)^2 \tag{3.22}$$

This leads to:

$$\frac{R}{R_0} = \frac{R}{\bar{R}(a=1)}\frac{\bar{R}(a=1)}{R_0} = 3\left(1 + 4\frac{\Omega_{\Lambda,0}}{\Omega_{M,0}}\right)\sqrt{\frac{f_{R0}}{f_R}} \tag{3.23}$$

For further use we will also need:

$$\sqrt{\frac{f_{R0}}{\bar{f}_R}} = \frac{\bar{R}}{\bar{R}(a=1)} = \frac{\left(\frac{1}{a^3} + 4\frac{\Omega_{\Lambda,0}}{\Omega_{M,0}}\right)}{\left(1 + 4\frac{\Omega_{\Lambda,0}}{\Omega_{M,0}}\right)} \tag{3.24}$$

So now we can proceed:

$$\begin{aligned} \delta\tilde{R} = \tilde{R} - \bar{\tilde{R}} = \frac{a^3}{R_0}(R - \bar{R}) = \frac{a^3}{R_0}\delta R = \\ = 3a^3\left(1 + 4\frac{\Omega_{\Lambda,0}}{\Omega_{M,0}}\right)\left[\sqrt{\frac{f_{R0}}{f_R}} - \frac{\left(\frac{1}{a^3} + 4\frac{\Omega_{\Lambda,0}}{\Omega_{M,0}}\right)}{\left(1 + 4\frac{\Omega_{\Lambda,0}}{\Omega_{M,0}}\right)}\right] \end{aligned} \tag{3.25}$$

So now let's consider the following substitution:

$$f_R = \bar{f}_R e^u \tag{3.26}$$

We see then that:

$$\frac{\delta\tilde{R}}{3} = a^3\left(\frac{1}{a^3} + 4\frac{\Omega_{\Lambda,0}}{\Omega_{M,0}}\right)\left(e^{-u/2} - 1\right) \tag{3.27}$$

From now on we will use only code quantities and drop the tilde notation. Expanding the Laplacian in code units we arrive at the following equation for f_R:

$$\bar{f}_R\frac{1}{r^2}\frac{\partial}{\partial r}\left(r^2\frac{\partial}{\partial r}e^u\right) = \frac{\Omega_{M,0}}{a\tilde{c}^2}\left[a^3\left(\frac{1}{a^3} + 4\frac{\Omega_{\Lambda,0}}{\Omega_{M,0}}\right)\left(e^{-u/2} - 1\right) - \delta\right] \tag{3.28}$$

Now we can make the observation that:

$$\frac{1}{r^2}\frac{\partial}{\partial r}\left(r^2\frac{\partial X}{\partial r}\right) = \frac{1}{r}\frac{\partial^2 X}{\partial r^2} \tag{3.29}$$

With that in mind let's consider a different substitution:

$$f_R = \frac{\bar{f}_R e^u}{r} \tag{3.30}$$

Thus we achieve the following equation:

$$\bar{f}_R\frac{1}{r}\frac{\partial^2}{\partial r^2}e^u = \frac{\Omega_{M,0}}{a\tilde{c}^2}\left[a^3\left(\frac{1}{a^3} + 4\frac{\Omega_{\Lambda,0}}{\Omega_{M,0}}\right)\left(\sqrt{r}e^{-u/2} - 1\right) - \delta\right] \tag{3.31}$$

Additionally we will convert it to a system of 2 first order ODEs using an auxiliary function:

$$y = \frac{\partial}{\partial r}e^u = e^u\frac{\partial}{\partial r}u = e^u u' \tag{3.32}$$

So the system with explicit r dependence looks like:

$$u'(r) = e^{-u(r)}y(r) \tag{3.33}$$

$$y'(r) = \frac{r}{\bar{f}_R}\frac{\Omega_{M,0}}{a\tilde{c}^2}\left[a^3\left(\frac{1}{a^3} + 4\frac{\Omega_{\Lambda,0}}{\Omega_{M,0}}\right)\left(\sqrt{r}e^{-u(r)/2} - 1\right) - \delta(r)\right] \tag{3.34}$$

Considering that we can approximate $r_{fi} \sim r_\infty$, where r_{fi} is the upper boundary of integration in code coordinates, we can impose the boundary condition that $f_R(r_{fi}) =$

$\bar{f}_R$ which translates to $u(r_{fi}) = \ln(r_{fi})$. As the relaxation scheme requires 2 boundary points we will impose a condition on the inner boundary. We do not know what the solution in the center of a collapsing isotropic mass distribution is. What we know is that it has to be symmetrical. Furthermore we can expect the solution to be smooth in the center. These 2 requirements imply that the derivative of the solution is zero in the center $f'_R(0) = 0$.

3.3 Relaxation scheme for solving the system of nonlinear ODEs

As discussed in [9] (p.8) the primary equation we need to solve is non-linear and cannot be solved as an initial value problem as the homogeneous equation has exponentially growing and decaying modes that get amplified by numerical errors. So we also employ a relaxation method for solving 2-point boundary problems in ODE. We employ a Newton's method [51] with dynamical allocation of the mesh grid. The mesh allocation function is taken to be logarithmic with its higher density at the origin, which is the primary region of interest and where we expect the solution to be more rapidly changing. As a guess solution for each step we utilize the relaxed solution of the previous step, while for the initial guess at the beginning of the simulation we use a linear solution. Generally if we have a system of discretized first order ordinary differential equations in the form:

$$0 = \mathbf{E}_k \equiv \mathbf{y}_k - \mathbf{y}_{k-1} - (x_k - x_{k-1})\mathbf{g}_k(x_k, x_{k-1}, \mathbf{y}_k, \mathbf{y}_{k-1}) \quad k = 2..M, \tag{3.35}$$

where the index k spans the number of grid points $2..M$, the vector $\mathbf{E}$ consists of the system of N discretized 1st order ODEs at each point (and has a total of $N * M$ components -

$N*(M-1)$ from differential equations and N from boundary conditions). $\mathbf{E}_1$ and $\mathbf{E}_{M+1}$ describe the boundary conditions. So a Taylor expansion with respect to small changes $\Delta\mathbf{y}_k$ looks like:

$$\mathbf{E}_k(\mathbf{y}_k+\Delta\mathbf{y}_k,\mathbf{y}_{k-1}+\Delta\mathbf{y}_{k-1})\approx \tag{3.36}$$
$$\approx \mathbf{E}_k(\mathbf{y}_k,\mathbf{y}_{k-1})+\sum_{n=1}^{N}\frac{\partial\mathbf{E}_k}{\partial y_{n,k-1}}\Delta y_{n,k-1}+\sum_{n=1}^{N}\frac{\partial\mathbf{E}_k}{\partial y_{n,k}}\Delta y_{n,k},$$

For a solution we want the updated value $\mathbf{E}_k(\mathbf{y}_k+\Delta\mathbf{y}_k,\mathbf{y}_{k-1}+\Delta\mathbf{y}_{k-1})$ to be zero, which sets up a matrix equation:

$$\sum_{n=1}^{N}S_{j,n}\Delta y_{n,k-1}+\sum_{n=N+1}^{2N}S_{j,n}\Delta y_{n,k}=-E_{j,k}, \tag{3.37}$$

where

$$S_{j,n}=\frac{\partial E_{j,k}}{\partial y_{n,k-1}},\quad S_{j,n+N}=\frac{\partial E_{j,k}}{\partial y_{n,k}}, \tag{3.38}$$

and the quantity $S_{j,n}$ is a $N\times 2N$ matrix at each point. Analogously we obtain similar algebraic equations on the boundaries. Considering our problem we look at Eqs. (3.33 and 3.34) to obtain (after discretization):

$$E_{1,k}=(y_k-y_{k-1})-(r_k-r_{k-1})\left(\frac{r_k+r_{k-1}}{2}\right)\frac{1}{\bar{f}_R}\frac{\Omega_{M,0}}{a\tilde{c}^2}* \tag{3.39}$$
$$*\left[a^3\left(\frac{1}{a^3}+4\frac{\Omega_{\Lambda,0}}{\Omega_{M,0}}\right)\left(\sqrt{\frac{r_k+r_{k-1}}{2}}e^{-(\frac{r_k+r_{k-1}}{4})}-1\right)-\delta(\frac{r_k+r_{k-1}}{2})\right]$$

$$E_{2,k}=(u_k-u_{k-1})-(r_k-r_{k-1})\left(\frac{y_k+y_{k-1}}{2}\right)e^{-(\frac{r_k+r_{k-1}}{2})} \tag{3.40}$$

$$S_{1,1,k}=-1,\quad S_{1,3,k}=1 \tag{3.41}$$

$$S_{1,2,k}=S_{1,4,k}=\left(\frac{r_k-r_{k-1}}{4}\right)\left(\frac{r_k+r_{k-1}}{2}\right)* \tag{3.42}$$
$$*\left[a^3\left(\frac{1}{a^3}+4\frac{\Omega_{\Lambda,0}}{\Omega_{M,0}}\right)\sqrt{\frac{r_k+r_{k-1}}{2}}e^{-(\frac{r_k+r_{k-1}}{4})}\right]$$

$$S_{2,1,k} = S_{2,3,k} = -\left(\frac{r_k - r_{k-1}}{2}\right) e^{-(\frac{r_k + r_{k-1}}{2})} \tag{3.43}$$

$$S_{2,2,k} = \left(\frac{r_k - r_{k-1}}{2}\right)\left(\frac{y_k + y_{k-1}}{2}\right) e^{-(\frac{r_k - r_{k-1}}{2})} - 1 \tag{3.44}$$

$$S_{2,4,k} = \left(\frac{r_k - r_{k-1}}{2}\right)\left(\frac{y_k + y_{k-1}}{2}\right) e^{-(\frac{r_k - r_{k-1}}{2})} + 1 \tag{3.45}$$

The boundary conditions are also easily translated in terms of the relaxation scheme.

$$E_{2,0} = e^{u_1} - r_1 y_1, \quad E_{1,M+1} = e^{u_M} - r_M \tag{3.46}$$

The notation here is probably a bit confusing. The quantity $\mathbf{E}$ is a vector which consists consecutively of 2 elements per $M-1$ grid points. In addition there is one element each at the beginning and the end that correspond to the boundary conditions. Thus the total length of $\mathbf{E}$ is NM, while the matrix S has $NM \times NM$ elements. The task of relaxing the solution at each step of the scheme requires solving the matrix equation $S \cdot \mathbf{b} = \mathbf{E}$. The vector $\mathbf{b}$ contains the updates $\Delta \mathbf{y}_k$. For a grid of 1000 points our equation requires a matrix of derivatives of size 2000x2000 elements. Fortunately it is sparsely populated and as such can be represented by a sparse array structure. This allows for the use of methods particularly designed for solving such systems, like Krylov's method, which we employ.

3.4 Dynamics

The time evolution of the simulation is employed in the usual way. At each time step we proceed as following:

1. Given an initial density profile (from the previous time step) we compute the corresponding solution for the f_R field.

2. This allows us to compute the solution for the Newtonian potential that drives the dynamics.

3. The mass shells are then moved according to the dynamics equations [12]:

$$\frac{d\tilde{r}}{da} = \frac{\tilde{p}}{\dot{a}a^2} \tag{3.47}$$

and

$$\frac{d\tilde{p}}{da} = -\frac{\nabla\tilde{\phi}}{\dot{a}}, \tag{3.48}$$

where $\dot{a} = a^{-1/2}\sqrt{\Omega_{M,0} + \Omega_{\Lambda,0}a^3}$, as we tune the expansion of the universe to be the same as in ΛCDM.

4. After the particles (shells) have been moved we can compute the new density distribution and proceed to a new time step thus closing the cycle.

3.5 Testing the code

An important issue in the case of numerical simulations is testing the code for stability and accuracy. The following have been checked:

1. Self consistency: as per [12] we can start with an analytical function for $f_R(r)$. This can be analytically solved to obtain a corresponding density distribution. Now we can plug that density distribution in the numerical code and check how well the obtained solution reproduces the original analytical function. We observe deviations of the order less than 10^{-7}.

2. During the relaxation scheme a measure of our accuracy is the residual relative size of the elements in the vector $\vec{b}$ (as compared to the size of the corresponding elements

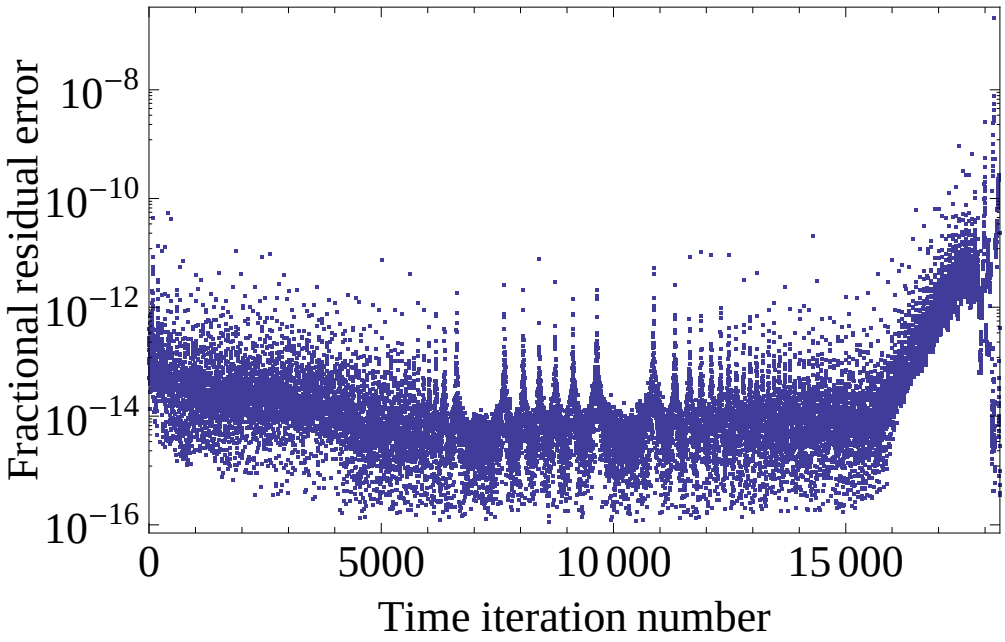

Figure 3.1: (Color online) Fractional change in the solution for f_R at the final step of the relaxation process .

of the solution) $\frac{\Delta \mathbf{y}_k}{\mathbf{y}_k}$. This tells us how much we need to correct the solution obtained by the previous step in the relaxation. A sample plot of these as a function of time iteration step is provided at Fig.3.1.

3. We have also checked that the dynamics of the simulation performs satisfactory for analytically solved situation. In particular we observe that for simulations of 20000 time iterations we recover the analytical results (turn around radius, virial radius, collapse time) for the Einstein-De Sitter (matter dominated $\Omega_m = 1$) model within 0.3%. This is the dominant numerical error.

3.6 The virialization problem.

An important issue we need to address before proceeding is of finding the epoch at which a collapsing object reaches its virial radius. In the cases of Einstein-De Sitter ($\Omega_{M,0} = 1$) and ΛCDM universes we have analytic solutions [11] (App. A), but that is not so in the case of f(R) gravity. What we do employ is a step by step calculation of the Virial condition. Let's look at energy conservation. The total velocity $v^t = dx/dt = d(ar)/dt = \dot{a}r + v$, where $x = ar$ is the physical distance, r is the comoving distance and $v = a\dot{r}$ is the proper peculiar velocity. The acceleration equation is

$$\frac{d(av_p)}{dt} = -\frac{d\phi}{dr} \tag{3.49}$$

On the other hand, v^t satisfies another equation

$$\dot{v^t} = -\frac{d\phi^t}{dx} \quad ; \quad \phi^t = \phi - \frac{1}{2}a\ddot{a}r^2 \tag{3.50}$$

Multiplying v^t to both sides and integrating over t, we obtain the familiar energy conservation

$$\frac{1}{2}(v^t)^2 + \phi^t = constant \tag{3.51}$$

For this reason, v^t and ϕ^t are the relevant quantities for the virial theorem. Multiply Eq. 3.50 by x, we obtain

$$\frac{d}{dt}(xv^t) - (v^t)^2 = -x\frac{d\phi^t}{dx} \tag{3.52}$$

This equation is satisfied at all time. After virialization, we then take the ensemble average of the above equation for each particle. Now the velocity of particles is random (no correlation with x), so we have $\langle xv^t \rangle = 0$. Then

$$\langle (v^t)^2 \rangle = \langle x\frac{d\phi^t}{dx} \rangle \tag{3.53}$$

An equivalent expression, which can be applied straightforwardly, is

$$2K \equiv \int (v^t)^2 dM = -\int x \frac{d\phi^t}{dx} dM \tag{3.54}$$

K is the total kinetic energy. The integral is over the region of mass M. This is the general expression of the virial theorem. One can check in the case of Newtonian gravity, $\phi^t \propto M/x$, this reduces to familiar form of the virial theorem, $2K + W = 0$. For the purposes of the simulation we need to express the above formulae in terms of comoving code coordinates Eqs. 3.13 and 3.14. It is straightforwards to obtain:

$$r_0^2 \int dM \left(\tilde{r}\dot{a} + \frac{H_0 \tilde{p}}{a} \right)^2 \tag{3.55}$$

for the kinetic term, and:

$$r_0^2 \int dM \tilde{r} \left(H_0^2 \frac{d\tilde{\phi}}{d\tilde{r}} - \tilde{r} a \ddot{a} \right) \tag{3.56}$$

for the potential term. These are subsequently discretized and the sum is over the region with relevant mass.

As expected in the case of GR (EDS and ΛCDM) the epoch at which the sum of these two terms is zero coincides with the analytically predicted epoch of reaching the virial radius [11, 54]:

$$\eta = \frac{\rho_{\text{eff}}}{(1+F)\rho_m} = \frac{2\Omega_\Lambda}{(1+F)\Omega_m a^{-3}(1+\delta)} \tag{3.57}$$
$$\eta = \frac{2s-1}{2s^3-1},$$

where $s = r_v/r_{TA}$ is the ratio of the virial radius and the maximal radius at turn-around. All relevant quantities are defined at turn-around.

In our simulations we observe that the difference between the analytical result and our evaluation is of order 10^{-5} for 20 000 time steps. We do not see any reason

for the same approach to not be valid in the case of f(R) modifications. Thus we define the epoch of achieving virial radius in $f(R)$ by the moment when this sum becomes zero during simulations. As per Fig. 3.2 observe that there are 2 moments when this condition is satisfied. We are obviously interested in the second one, which occurs after passing the turnaround point.

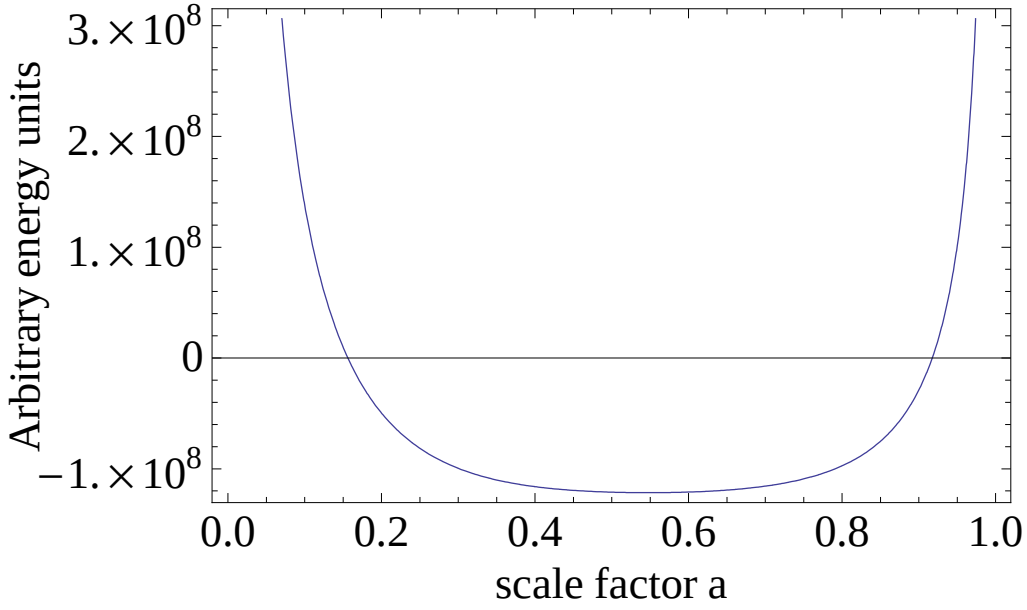

Figure 3.2: (Color online) Evolution of the virial term. Observe that there are two points where it crosses the zero. We are interested in the one that happens after turnaround.

3.7 First light: the edge effect

When people study spherical collapse in ordinary GR they concentrate on initial top-hat density distributions. This is very convenient as a top-hat remains a top-hat during collapse. (In other words a top-hat is a Green's function for the spherical collapse evolution operator in GR). This allows for a straight forwards definition of fundamental quantities

of spherical collapse - in particular δ_c and Δ_{vir}. This is not the case for modified gravity theories. Unfortunately we have no idea what profile would be the analogous Green's function. We can still compare, though, the evolution of top-hat distribution and try to compute δ_c and Δ_{vir} in a similar way. The issue we encountered was that of an edge effect: at the outer edge of the initial distribution the density becomes very large. This effect is easy to explain. As the universe expands the size of the background f_R field increases and we approach the high limit of the $f(R)$ theory - where it behaves as GR with enhanced Newton's constant. This means that the outer edge of the collapses faster than it would do in regular GR. The inside of the collapsing object, though, is under the effect of the chameleon and the solution for the f_R field becomes much smaller and thus the collapse slows down to approach the one in GR with regular strength of the Newton's constant. This makes the edge to become more and more dense as compared to the inside of the object. And this creates a positive feedback. The higher the edge density the stronger its screening effect and the inside slows down even further thus enhancing the accumulation of matter at the edge.

There is an even more interesting consequence as Justin Khoury has suggested. The mathematics of the chameleon is such that this edge effect can separate the inside and the edge with a void. We actually observe that the solution for f_R starts exhibiting that kind of behavior in the very late stages of the collapse but it's very close to the epoch of reaching virial radius so the effect is unobservable in the density profiles.

The edge effect unfortunately has some very adverse effects. Our simulation code became irreparably (at least for us) unstable in the very late stages of the collapse of pure top-hat distribution. What we could do though was to smooth out the edge which

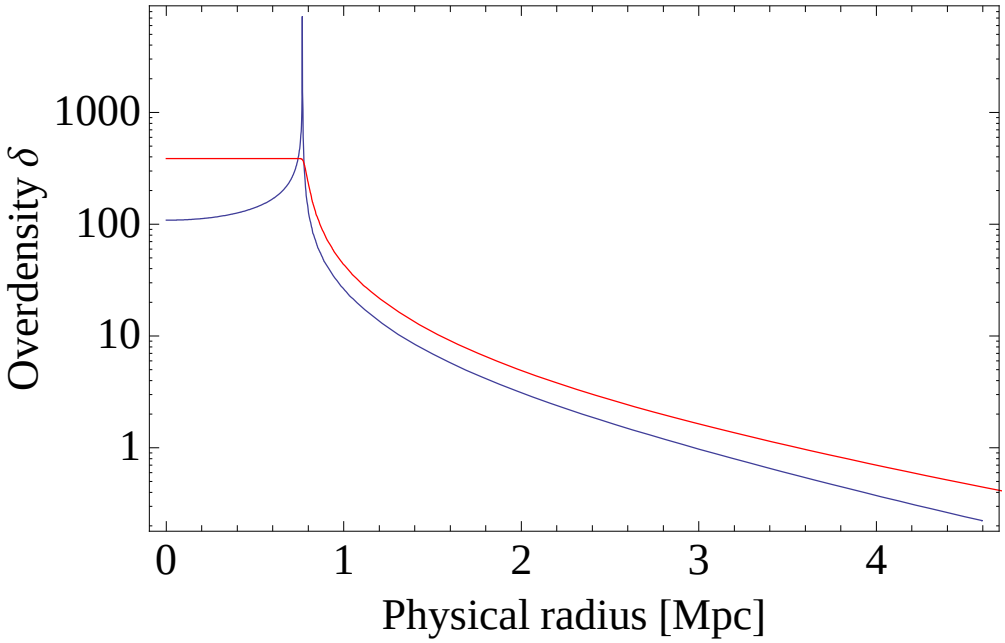

Figure 3.3: (Color online) a comparison of the density profiles at the epoch of achieving virial radius between $f(R)$ and ΛCDM. In each case the starting profile and mass are the same. The virial radius is reached at different epochs. The ΛCDM profile is in red.

reduces the strength of the positive feedback and allows for stable evolution of the collapse. The complicated part of that approach is that, as Birkhoff's theorem is not satisfied in $f(R)$ models of gravity, the end result significantly depends on the environment, and in particular, what smoothing is used.

In our case we appropriate a Gaussian, which has the benefit of being smooth at the seem. The dispersion of the Gaussian allows for controlling how close we are to a pure top-hat density distribution. Even with smoothing, though, the code becomes unstable beyond reaching the epoch of the virial radius, preventing us from achieving collapse to singularity - the epoch of collapse. In Fir. 3.3 we show a comparison of the density profiles at virialization between $f(R)$ and ΛCDM. In each case the starting profile and mass are the same. They achieve virialization at different epochs.

3.8 Spherical collapse of top-hat initial distributions. Measuring δ_c.

The main goal of this study is to compare the non-linear evolution of spherical collapse with what previous research in the field predicted.

3.8.1 The expectations: what was previously known.

The precursor paper to our study [11] dealt with spherical collapse in an analytical way (App.A) by solving the 2 limiting cases for the strength of the effective Newton's constant in the $f(R)$ model of gravity. The prediction in the end is that the fundamental quantities should lie inside of the region bound by the values of the 2 limiting cases. In particular they are identified by the value of the parameter F which governs the strength

of the effective Newton's constant. Regular GR corresponds to $F = 0$ and the strong field limit to $F = 1/3$. For $\Omega_{M,0} = 0.24$ these imply $\delta_c = 1.673$ for $F = 0$, and $\delta_c = 1.692$ for $F = 1/3$.

3.8.2 Computing δ_c

Generally computing δ_c is straight forward. For a given starting epoch a_{in} we need to find an initial overdensity $\delta_{in,GR}$, which would collapse to a singularity at present time. Then we just need to evolve that initial overdensity to present time via the linear growth factor. In the case of ΛCDM this can be performed analytically ([55] App.A). In the case of $f(R)$ modified gravity there are 2 complications.

1. The linear growth factor is scale dependent.

2. Our simulation allows us to only reach the epoch of achieving the virial radius and not the epoch of collapse.

Resolving the first issue is not a complicated task. The solution is to go to Fourier space and convolve the linear growth factor at the epoch of collapse (normalized with the growth factor at the initial epoch) with the Fourier image of a top-hat function. After that, we need to Fourier transform back to physical space, which is greatly simplified, as we are interested only at the value at $r = 0$, and sums up to the evaluation of an integral. In the next subsection we deal with the problem of estimating the collapse epoch.

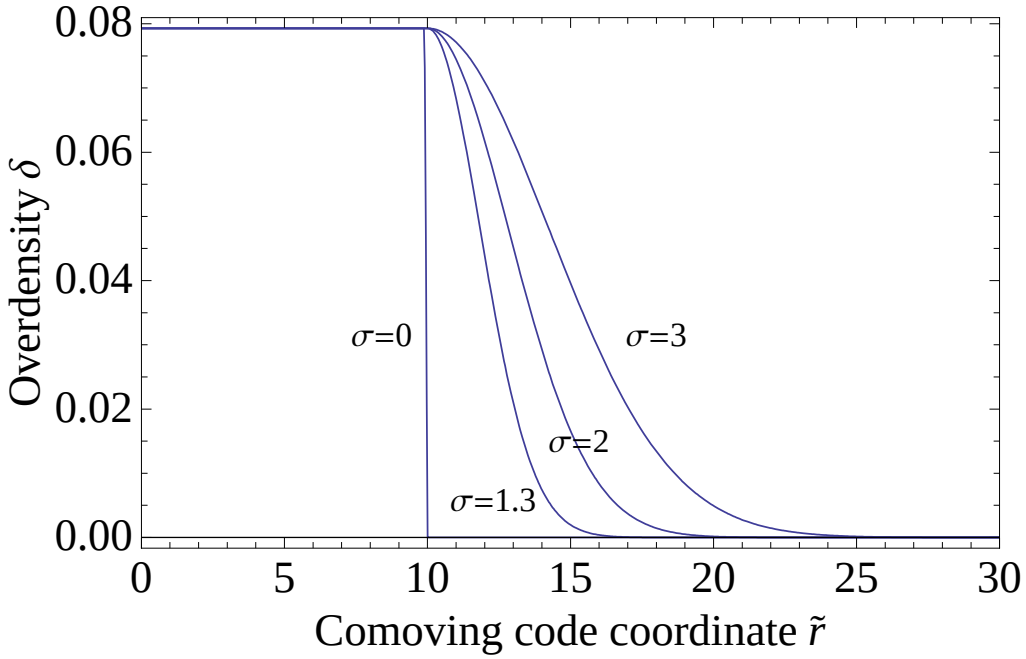

Figure 3.4: (Color online) Smoothed density profiles with Gaussians with different dispersion.

3.8.3 Environmental dependence. How to approximate a top-hat initial distribution.

The numerical issues we have with the development of the edge-effect - the strong spike - are a significant obstacle in obtaining quantified results. But the approach we employ to at least partially resolve the conundrum allows us to also study the environment effects due to the invalidity of Birkhoff's theorem. Recall that if Birkhoff's theorem is valid in a gravitational theory then the behavior of a shell depends only on the mass inside the ball enclosed by that shell. In our case that is not correct and shells are influenced by what is outside - the environment. We utilize a sequence of initial profiles, each of which has a pure top-hat part and then is smoothed with a Gaussian with varying dispersions Fig.3.4 that bring us closer and closer to a pure top-hat distribution. This way we can

study the trend of changes in the top-hat part of the initial profile when approaching a pure top-hat overdensity.

3.8.4 Finding the epoch of collapse - going beyond the epoch of achieving the virial radius.

As mentioned before beyond the virial epoch our code experiences numerical instabilities due to the edge effect spike in the overdensity. So we need to find a way to estimate the collapse epoch. The first observation we make is that the time/scale factor between the epoch of reaching the virial radius and the epoch of collapse to singularity is a small fraction of the total time/scale factor spent in the evolution of the spherical object. Thus we will assume that if an object in $f(R)$ gravity achieves its virial radius at the same epoch as a corresponding object in ΛCDM does, then these two objects should reach collapse to a singularity at approximately the same epoch as well. Then we can make an estimate of how wrong we are in this prediction. The task of finding δ_c then is moved to finding the initial overdensity in $f(R)$, which would reach its virial radius at the same epoch at which a corresponding object in GR does. In addition we require that the GR object collapses to a singularity at the present epoch.

What is left is estimating the error of this calculation. One way to approach the the problem is to look at the radial velocity field of the evolving shells in our simulation and compare them between the corresponding objects in $f(R)$ and ΛCDM. On Pic. 3.5 we show the velocity ratio computed shell by shell and normalized by the physical position of the shells (the corresponding $f(R)$ and ΛCDM have different mass and different size at the epoch of achieving the virial radius). The different colors correspond to the different

smoothing factors we have introduced as way to approach a pure top-hat distribution. In our simulation we have chosen shell number 100 to represent the edge of the top-hat part of the initial overdensity. As we can see the normalized velocity ratio remains within 5% of unity, which suggests that a good estimate of our error would be of the same order.

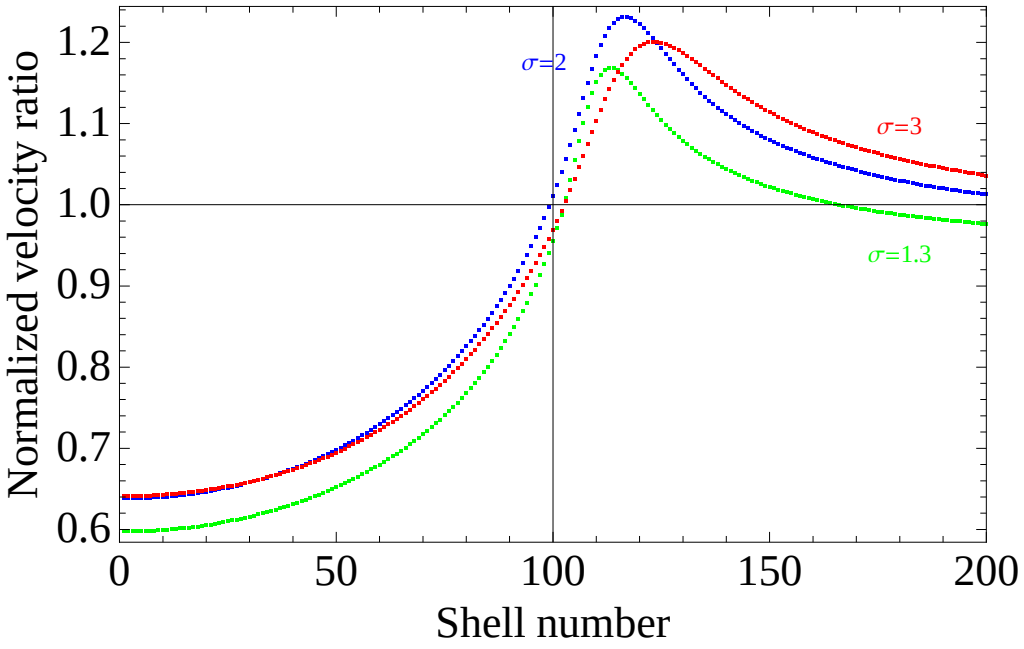

Figure 3.5: (Color online) Shell by shell velocity ratio of $f(R)$ and ΛCDM collapsing objects, normalized by the physical position of the corresponding shells. Dependence on smoothing factor is shown by different colors (red for $\sigma = 3$, blue for $\sigma = 2$, and green for $\sigma = 1.3$). Edge of the top-hat part of the initial distribution is represented by shell number 100.

Another way to approach the issue is to vary the initial overdensity and look at how much it changes the epoch of achieving the virial radius and compare with the expected epoch of collapse. In particular, values for the initial overdensity, that have epoch of virial radius close or beyond the expected epoch of collapse, set a bound on our error. We found that this also puts a hard error bar of 5%, which is what we finally used in our calculation.

3.8.5 Results and discussion.

The main result of the work is presented in Fig.3.6. The calculations are done for $\Omega_m = 0.24$ to be able to directly compare results with [11]. We needed to check the following conjectures:

1. In the weak field regime our calculations should approach the result for regular strength ΛCDM ($F = 0$).

2. In the strong field regime the result must approach the values predicted in [11] for $F = 1/3$.

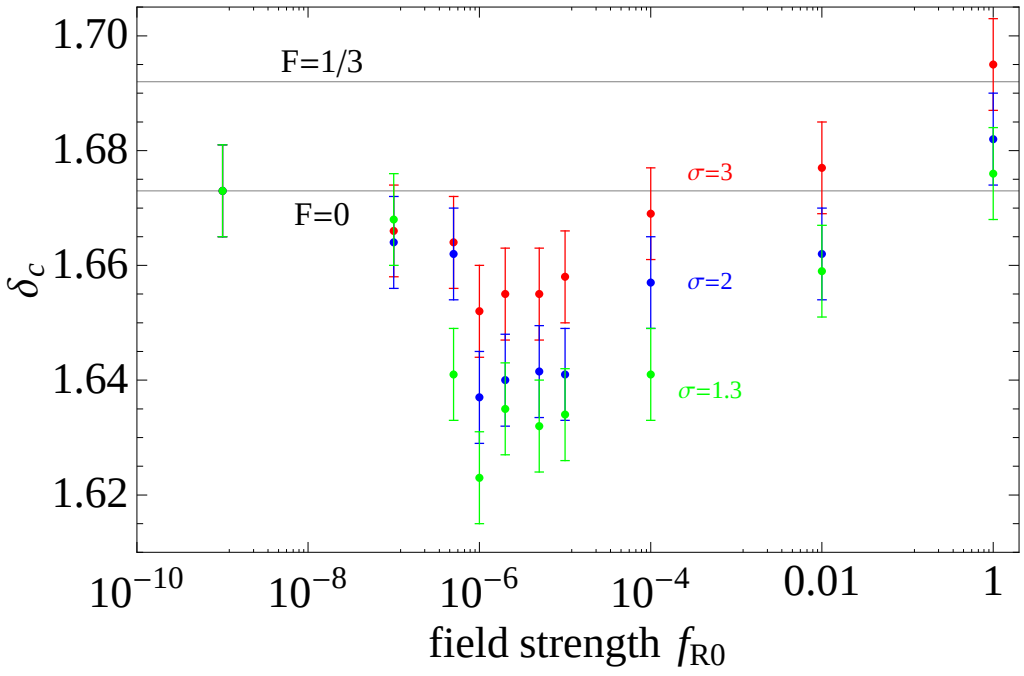

Figure 3.6: (Color online) δ_c as a function of field strength f_{R0}, $\Omega_{M,0} = 0.24$.

These conjectures have been confirmed successfully. The new result is the behavior in the mid-range of field strength, and particularly in the physically interesting region around

$f_{R0} = -10^{-6}$ – currently the upper bound on that parameter that has not been rejected by observations or theoretical considerations. We observe strong environmental dependence with a significant trend: when reducing the dispersion of the smoothing Gaussian (and thus approaching pure top-hat distribution) we deviate further away from the analytical prediction in [11]. This result shows that the non-linear chameleon properties of the $f(R)$ models strongly affect its behavior and linear predictions should be viewed as simple guidelines.

It is important to point out that the spiked edge-effect observed in the behavior of top-hat initial density distributions is not an automatic rejection of the model. In reality we know that large-scale structure did not evolve from top-hat distributions. In our simulations we also look at more realistic initial profiles – for example pure Gaussian distribution – and they do not exhibit extraordinary behavior. We focused on top-hat for this work as we wanted to obtain some quantified initial results from the simulation.

3.9 Future work.

Obtaining estimates for δ_c is the first step of the possible applications of our simulation. We intend to continue our work with the computation of the virial overdensity Δ_{vir} and then focus on abundance and clustering properties of halos: mass function and halo bias. In addition, we would also extend our results across a wider range of cosmological parameters (Ω_m for example).

Acknowledgments: We are grateful to Wayne Hu, Mike Jarvis, Justin Khoury, Matt Martino, and Ravi Sheth. BJ is supported in part by NSF grant AST-0607667.

Chapter 4

Weak lensing Responsivity.

4.1 Introduction

One of the most powerful tools for studying the distribution of matter in the Universe is the gravitational lensing of light. While the so-called strong lensing, which produces phenomena like multiple images, arcs, and Einstein rings, contributes a lot of information about rich galaxy clusters, cosmologists are interested in the properties of more typical mass structures. To characterize these, weak gravitational lensing can be used, where the distortions of shapes of a large number of background galaxies is analyzed. These signals are very subtle: the typical shears and magnifications are of order a few percent. In addition the original undistorted images are unobservable and thus the useful signal is just a perturbation over an intrinsic variation of the shapes of the galaxies of 30% or more. A study of some optimal techniques for the measurement of the weak gravitational shear from cosmological images was done in [14]. A major topic in that study is how from a set of galaxy elipticities $\tilde{\mathbf{e}}_\mathbf{i}$ with known measurement error to obtain

a best estimate of the lensing distortion $\boldsymbol{\delta}$. This task depends on several factors: how the original ensemble of elipticities responds to the applied distortion, the *shape noise* coming from the variety of shapes in the unlensed population, and the measurement error for each galaxy. The general approach is to a create statistics $\tilde{\boldsymbol{\delta}}$ from the $\tilde{\mathbf{e}}_\mathbf{i}$ to estimate the lensing distortion $\boldsymbol{\delta}$ that has been applied. We know that for weak lensing ($|\boldsymbol{\delta}| << 1$) elipticities behave like (3.29 in [14]):

$$\mathbf{e}(\boldsymbol{\delta}) \approx \mathbf{e} + \boldsymbol{\delta} - \mathbf{e}(\boldsymbol{\delta} \cdot \mathbf{e}) \tag{4.1}$$

This means we need to know the "Responsivity" of the statistics defined as:

$$\tilde{R} = \frac{\partial \tilde{\boldsymbol{\delta}}}{\partial \boldsymbol{\delta}} \tag{4.2}$$

In what follows, we outline the derivation in [14]. See their section 5 for more details. Generally a galaxy image with true elipticity $\mathbf{e}$ will be measured at $\tilde{\mathbf{e}}$ with probability distribution $p(\tilde{\mathbf{e}}|\mathbf{e})$. So the measured distribution of elipticities under lensing distortion $\boldsymbol{\delta}$ is:

$$\tilde{P}_{\boldsymbol{\delta}}(\tilde{\mathbf{e}}) = \int d^2e \, P_{\boldsymbol{\delta}}(\tilde{\mathbf{e}}) \, p(\tilde{\mathbf{e}}|\mathbf{e}) \tag{4.3}$$

We assume distortion of the form:

$$\tilde{\boldsymbol{\delta}} = \frac{\sum w(\tilde{\mathbf{e}}_\mathbf{i}) \, \tilde{\mathbf{e}}_\mathbf{i}}{\sum w(\tilde{\mathbf{e}}_\mathbf{i})} = \frac{\int d^2\tilde{e} \, w(\tilde{\mathbf{e}}) \, \tilde{P}(\tilde{\mathbf{e}}) \, \tilde{\mathbf{e}}}{\int d^2\tilde{e} \, w(\tilde{\mathbf{e}}) \, \tilde{P}(\tilde{\mathbf{e}})} \tag{4.4}$$

Additionally we assume isotropic population thus terms linear in e_+ or $e_\times$, where $\mathbf{e} \equiv (e_+, e_\times) \equiv (e\cos\theta, e\sin\theta)$ and similarly for $\boldsymbol{\delta}$, can be dropped and also:

$$R = \frac{\partial \tilde{\delta}_+}{\partial \delta_+} = \frac{\partial \tilde{\delta}_\times}{\partial \delta_\times}, \tag{4.5}$$

and all the off-diagonal elements are zero. Then we get:

$$\langle R \rangle = \frac{\int d^2\tilde{e} \, \left[w(\tilde{e}) \tilde{e}_+ \int d^2e \, p(\tilde{\mathbf{e}}|\mathbf{e}) \left(\frac{\partial P_{\boldsymbol{\delta}}(\tilde{\mathbf{e}})}{\partial \delta_+} \right) \right]}{\int d^2\tilde{e} \, w(\tilde{e}) \, \tilde{P}(\tilde{e})} \tag{4.6}$$

Here w is a weight function for combining elipticities into distribution. Using (5.6) in [14] which gives us $P_{\boldsymbol{\delta}}(\tilde{\mathbf{e}}) = P(\mathbf{e})[1 + \boldsymbol{\delta}.\mathbf{e}(3 - \frac{1-e^2}{e}\frac{d\log P}{de})]$ we obtain:

$$\langle R\rangle = \frac{\int d^2\tilde{e}\,\left[w(\tilde{e})\tilde{e}_+ \int d^2e\, p(\tilde{\mathbf{e}}|\mathbf{e})P(\mathbf{e})\, e_+\,(3 - \frac{1-e^2}{e}\frac{d\log P}{de})\right]}{\int d^2\tilde{e}\, w(\tilde{e})\,\tilde{P}(\tilde{e})} \tag{4.7}$$

Finally we need an expression for R as a sum over the observed objects and applied weights. For this we take the derivative of (4.4) and assume that the measurement error does not have first order dependence on δ (which is a good approximation).

$$R = \frac{\sum(w(1 - \langle e_+^2\rangle_{\tilde{e}} + \frac{\tilde{e}_+^2}{\tilde{e}}\frac{dw}{d\tilde{e}}(1 - \langle e_+^2\rangle_{\tilde{e}} - \langle e_+e_\times\rangle_{\tilde{e}}\frac{\tilde{e}_\times}{\tilde{e}_+}))}{\sum w}, \tag{4.8}$$

where

$$\langle e_+^2\rangle_{\tilde{e}} = \int d^2e\, p(\mathbf{e}|\tilde{\mathbf{e}})\, e_+^2 = \frac{\int d^2e\, p(\tilde{\mathbf{e}}|\mathbf{e})P(e)e_+^2}{\int d^2e\, p(\tilde{\mathbf{e}}|\mathbf{e})P(e)}, \tag{4.9}$$

and analogously for $\langle e_+e_\times\rangle_{\tilde{e}}$. In [14] a fairly simple approximation for $P(e)$ was made. Our goal is to improve upon this by allowing for the calculation of the integral for more realistic $P(e)$.

4.2 Calculating the integral

We assume a Gaussian for $p(\tilde{\mathbf{e}}|\mathbf{e}) = \frac{1}{\sqrt{2\sigma_\mu^2}}e^{-\frac{(\tilde{\mathbf{e}}-\mathbf{e})^2}{2\sigma_\mu^2}}$. Then the relevant quantity we are interested in is: $\langle e_+^2\rangle_{\tilde{e}} = \frac{A}{B}$, where we obtain the following integrals by switching to polar coordinates in (4.9).

$$A = \frac{1}{\sqrt{2\sigma_\mu^2}}\int_0^{2\pi} d\Phi \int_0^1 de\, e^3\cos^2(\Phi)P(e)* \tag{4.10}$$
$$* e^{-\frac{\tilde{e}^2}{2\sigma_\mu^2}} e^{\left[-\frac{e^2}{2\sigma_\mu^2}+\frac{2e}{2\sigma_\mu^2}(\tilde{e}_1\cos(\Phi)+\tilde{e}_2\sin(\Phi))\right]}$$

$$B = \frac{1}{\sqrt{2\sigma_\mu^2}} \int_0^{2\pi} d\Phi \int_0^1 de\, e\, e^{-\frac{\tilde{e}^2}{2\sigma_\mu^2}} e^{\left[-\frac{e^2}{2\sigma_\mu^2} + \frac{2e}{2\sigma_\mu^2}(\tilde{e}_1 \cos(\Phi) + \tilde{e}_2 \sin(\Phi))\right]} P(e) \tag{4.11}$$

So let's deal with the angular parts of the integrals first. We have for B:

$$\int_0^{2\pi} d\Phi\, e^{\frac{2e\tilde{e}}{2\sigma_\mu^2}\cos(\Phi-\theta)} = 2\pi\, e^{-\frac{e^2}{2\sigma_\mu^2}} I_0(\frac{\tilde{e}e}{\sigma_\mu^2}), \tag{4.12}$$

where we have expressed $\tilde{\mathbf{e}}$ in polar coordinates too. This allows us to obtain:

$$B = \frac{e^{-\frac{\tilde{e}^2}{2\sigma_\mu^2}}}{\sqrt{2\sigma_\mu^2}} \int_0^1 de\, e\, P(e)\, 2\pi\, e^{-\frac{e^2}{2\sigma_\mu^2}} I_0(\frac{\tilde{e}e}{\sigma_\mu^2}), \tag{4.13}$$

where I_n are the modified Bessel functions. In this form this integral can be easily computed numerically. The analogous integral for A is:

$$\int_0^{2\pi} d\Phi \cos^2(\Phi) e^{\frac{2e}{2\sigma_\mu^2}(\tilde{e}_1 \cos(\Phi) + \tilde{e}_2 \sin(\Phi))} = \int_0^{2\pi} d\Phi \cos^2(\Phi)\, e^{\frac{2e\tilde{e}}{2\sigma_\mu^2}\cos(\Phi-\theta)}. \tag{4.14}$$

Denoting $k = \frac{\tilde{e}e}{\sigma_\mu^2}$ gives us:

$$\int_0^{2\pi} d\Phi \cos^2(\Phi)\, e^{k\, \cos(\Phi-\theta)}$$

Now change coordinates to:

$$x = \Phi - \theta \;\Rightarrow\; \Phi = x + \theta \tag{4.15}$$

$$\cos^2(x+\theta) = \frac{1}{2}[1 + \cos(2x+2\theta)] = \frac{1}{2}[1 + \cos(2x)\cos(2\theta) - \sin(2x)\sin(2\theta)] \tag{4.16}$$

Thus we get the following expression:

$$\int_{-\theta}^{2\pi-\theta} dx\, \frac{1}{2}[1 + \cos(2x)\cos(2\theta) - \sin(2x)\sin(2\theta)]\, e^{k\, \cos(x)} \tag{4.17}$$

One piece of the integral:

$$\int_{-\theta}^{2\pi-\theta} dx\, \sin(2x)\sin(2\theta)\, e^{k\, \cos(x)} = 0$$

is zero by symmetry argument. So after changing back the domain of integration (as it is a full period) we are left with:

$$\int_0^{2\pi} dx\, \frac{1}{2}\left[1+\cos(2x)\cos(2\theta)\right]\, e^{k\,\cos(x)} = \pi\left[I_0(\frac{\tilde{e}e}{\sigma_\mu^2}) + \cos(2\theta) I_2(\frac{\tilde{e}e}{\sigma_\mu^2})\right] \tag{4.18}$$

Or we get:

$$A = \frac{e^{-\frac{\tilde{e}^2}{2\sigma_\mu^2}}}{\sqrt{2\sigma_\mu^2}} \int_0^1 de\, e^3\, P(e)\, \pi\, e^{-\frac{e^2}{2\sigma_\mu^2}} \left[I_0(\frac{\tilde{e}e}{\sigma_\mu^2}) + \cos(2\theta) I_2(\frac{\tilde{e}e}{\sigma_\mu^2})\right] \tag{4.19}$$

We have another term in the expression for the Responsivity to calculate: $\langle e_+ e_\times \rangle_{\tilde{e}}$ We can analogously express it as the ratio of two integrals $\frac{C}{B}$ where B is the same as before and for C we have:

$$C = \frac{1}{\sqrt{2\sigma_\mu^2}} \int_0^{2\pi} d\Phi \int_0^1 de\, e^3 \cos(\Phi)\sin(\Phi) P(e) * \tag{4.20}$$
$$* e^{-\frac{\tilde{e}^2}{2\sigma_\mu^2}} e^{\left[-\frac{e^2}{2\sigma_\mu^2} + \frac{2e}{2\sigma_\mu^2}(\tilde{e}_1\cos(\Phi) + \tilde{e}_2\sin(\Phi))\right]}$$

Once again we will calculate the angular part of the integral with the same change of coordinates (4.15):

$$\begin{aligned} &\frac{1}{2}\int_0^{2\pi} d\Phi \sin(2\Phi)\, e^{k\,\cos(\Phi-\theta)} = \\ &\frac{1}{2}\int_{-\theta}^{2\pi-\theta} dx\, \left[\sin(2x)\cos(2\theta) + \cos(2x)\sin(2\theta)\right] e^{k\,\cos(x)} \\ &= \pi \sin(2\theta) I_2(k). \end{aligned} \tag{4.21}$$

Here again the first term is zero by symmetry argument and the second one just integrates to a modified Bessel function. So the final result is:

$$C = \frac{e^{-\frac{\tilde{e}^2}{2\sigma_\mu^2}}}{\sqrt{2\sigma_\mu^2}} \int_0^1 de\, e^3\, P(e)\, \pi\, e^{-\frac{e^2}{2\sigma_\mu^2}} \sin(2\theta) I_2(\frac{\tilde{e}e}{\sigma_\mu^2}) \tag{4.22}$$

We can now express these expressions in a better form (5.32 in [14]).

$$\langle e_+^2 \rangle_{\tilde{e}} = k_0(\tilde{e}) + k_1(\tilde{e})\tilde{e}_+^2 \tag{4.23}$$

$$\langle e_+ e_\times \rangle_{\tilde{e}} = k_1(\tilde{e})\tilde{e}_+\tilde{e}_\times, \tag{4.24}$$

where k_0 and k_1 depend only on the magnitude and not the direction of $\tilde{\mathbf{e}}$. After substituting the expressions we calculated and a slight manipulation we obtain:

$$k_0(\tilde{e}) = \frac{1}{2}\frac{\int_0^1 de\, e^3\, P(e) e^{-\frac{e^2}{2\sigma_\mu^2}} \left[I_0(\frac{\tilde{e}e}{\sigma_\mu^2}) - I_2(\frac{\tilde{e}e}{\sigma_\mu^2}) \right]}{\int_0^1 de\, e\, P(e) e^{-\frac{e^2}{2\sigma_\mu^2}} I_0(\frac{\tilde{e}e}{\sigma_\mu^2})} \tag{4.25}$$

$$= \frac{\sigma_\mu^2}{\tilde{e}}\frac{\int_0^1 de\, e^2\, P(e) e^{-\frac{e^2}{2\sigma_\mu^2}} I_1(\frac{\tilde{e}e}{\sigma_\mu^2})}{\int_0^1 de\, e\, P(e) e^{-\frac{e^2}{2\sigma_\mu^2}} I_0(\frac{\tilde{e}e}{\sigma_\mu^2})} \tag{4.26}$$

$$k_1(\tilde{e})\tilde{e}^2 = \frac{\int_0^1 de\, e^3\, P(e) e^{-\frac{e^2}{2\sigma_\mu^2}} I_2(\frac{\tilde{e}e}{\sigma_\mu^2})}{\int_0^1 de\, e\, P(e) e^{-\frac{e^2}{2\sigma_\mu^2}} I_0(\frac{\tilde{e}e}{\sigma_\mu^2})} \tag{4.27}$$

We have used the recurrence relationship for the modified Bessel functions to produce the final result for $k_0(\tilde{e})$.

With these coefficients our expression for the Responsivity (4.8) becomes:

$$R = \frac{\sum \left[w \left(1 - k_0 - \frac{k_1 \tilde{e}^2}{2} \right) + \frac{\tilde{e}}{2}\frac{dw}{d\tilde{e}} \left(1 - k_0 - k_1 \tilde{e}^2 \right) \right]}{\sum w} \tag{4.28}$$

4.3 Numerical computation

4.3.1 The probability function

As mentioned above the simplification of the integrals from $2D$ to $1D$ allows for a much faster numerical computation and thus we can examine the results with several

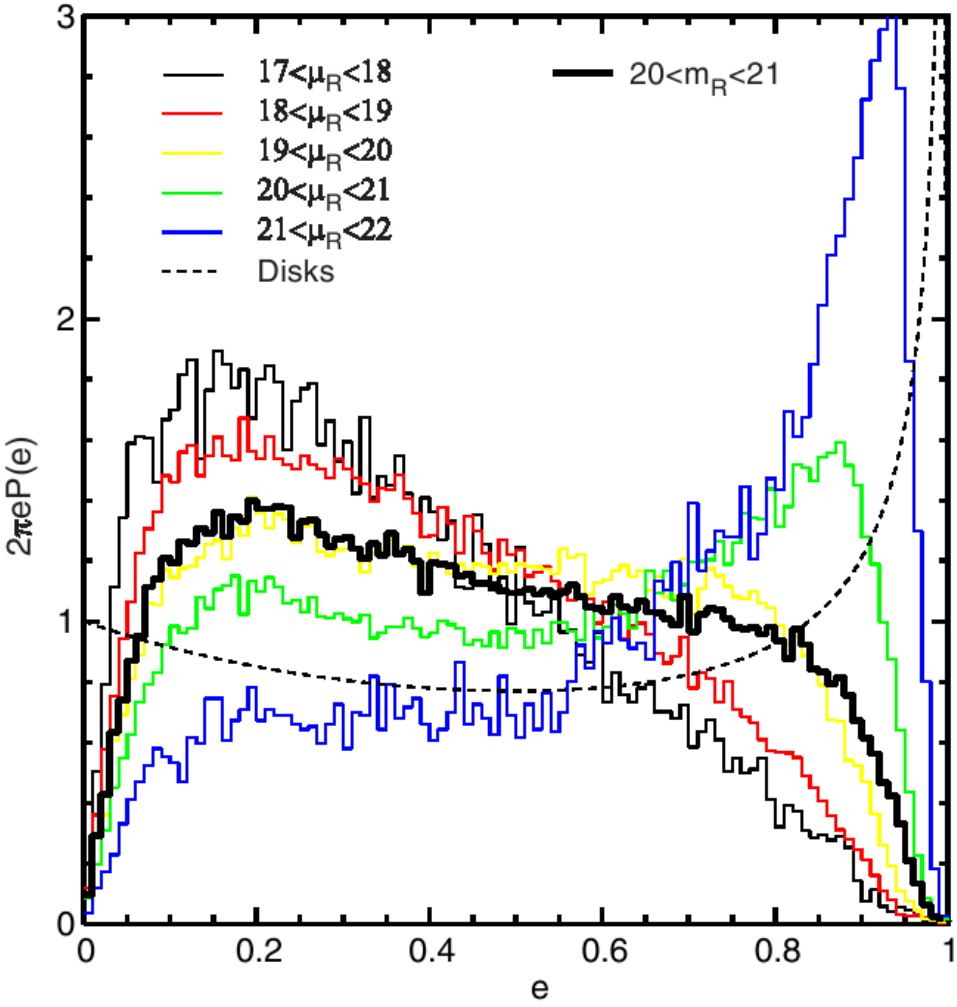

Fig. 4.— The distribution of intrinsic ellipticities for modestly bright galaxies ($m_R \approx 20$) is plotted; we plot $2\pi eP(e)$ rather than $P(e)$ as the nature of the population is more apparent. The distribution is highly dependent upon surface brightness μ_R, presumably reflecting the difference between spheroid- and disk-dominated galaxies. The dashed line is the distribution for an isotropic population of circular disks. The high-μ galaxies are more useful for distortion measurements. The heavy histogram combines all surface brightnesses in the magnitude range $20 < m_R < 21$. Though it is difficult to tell from this plot, $P(e)$ is finite and increasing as $e \to 0$. Optimal weighting takes advantage of this structure to reduce the noise in the distortion measurement.

Figure 4.1: (Color online) The distribution of intrinsic elipticities for modestly bright galaxies.

possible assumptions for $2\pi eP(e)$ and compare them with the analytically treatable case of Gaussian distribution. One such assumption is to simulate the distribution presented in Fig. 4.1 (Fig.4 taken from [14], heavy histogram) with the following expression:

$$P(e) = \frac{1}{2\pi}[C_1 H(\epsilon - e) + (\frac{C_2}{e} + C_3)H(e - \epsilon)H(\mu - e) + C_4(\frac{1-e}{e})H(e - \mu)], \quad (4.29)$$

where $H(x)$ is the Heaviside function and $C_1, ..., C_4, \epsilon, \mu$ parametrise the distribution. The particular choice of values we took is $C_1 = 12.0$, $C_2 = 1.24$, $C_3 = -0.4$, $C_4 = 6.0$, $\epsilon = 0.1$, $\mu = 0.85$, which provide a good approximation to the observed $P(e)$ of the real galaxies shown in Fig. 4.1.

4.3.2 Description of the simulation

We start with creating a set of galaxies with random distribution in elipticities. This is achieved by the following steps:

a) We pick out the magnitude of the original "true" elipticity from the suggested probability function $P(e)$. (For the case of old k's this function is approximated by a Gaussian with dispersion equal to the shape-noise error. This allowed for analytical solution to the Responsivity integrals). In our case we make a "better" approximation to the observed probability function (the function described above). After the magnitude is picked out from that distribution the direction of the elipticity is randomly chosen (as we assume isotropy).

b) The weak lensing shear is chosen. In particular we pick a specific magnitude of the shear with some random direction. The question is can we predict the applied weak lensing.

c) Finally we apply measurement error. We allow a range of dispersions for the Gaussian distributed error. For each galaxy we randomly pick dispersion from that range. Then we pick the specific magnitude and direction of the error from a Gaussian distribution with that dispersion.

After all previous steps we arrive at the the "observed" galaxy. We create a large set of those (usually 10^6 but simulations with 10^7 and 10^8 galaxies are also done). The next step is to perform the integrals needed to calculate the Responsivity. For each galaxy we obtain the k_0 and k_1 quantities, both with the numerical $1D$ integrals (new k's) and the old analytical formulae (old k's). Then Responsivity is calculated. For that we have explored 3 different weighting schemes.

a) Uniform scheme ($w = 1$ for all galaxies).

b) Elipticity dependent scheme (favors low elipticities). Observed and known to have bias for large (> 0.1) shears. In our simulations we use relatively large shears (up to 0.3) and so we used the final weighting scheme.

c) Non-elipticity dependent scheme.

$$w = \frac{1}{\sigma_{SN}^2 + \sigma_{\mu}^2} \tag{4.30}$$

This scheme favors low measurement error galaxies. It simplifies the calculation of the Responsivity (as $\frac{dw}{d\bar{e}} = 0$) as well as makes it easier for analytical dissection of the results (via δ-function distribution for $P(e)$ which allows immediate analytical solution for all integrals and thus for a way to make a proof check of the code.) After the Responsivity is calculated we find our predicted weak lensing shear as the mean elipticity divided by the Responsivity. From that we can obtain the magnitude of the predicted weak lensing

shear.

4.3.3 Comparison of old k's and new k's results

We need to establish the method of comparison. The way we chose to do it is the following: We perform the simulations and calculations for a range of magnitudes of the applied weak lensing shear (with random directions). At the end this creates a set of true vs predicted shears with their uncertainties. Then we attempt a linear fit for this set. If the model is working we should get a good fit with slope of 1 (and intercept of 0). How close our calculations are to having a slope of 1 (within uncertainty) tells us how good the model is.

The most important result we obtained with the current code is the following: The simulation contains 10^7 galaxies per point. The range of measurement uncertainties is 0.001 to 0.5. The elipticity probability function is (4.29). The linear fit has 11 data points for magnitude of the applied shear from 0 to 0.3, spread equidistantly with stepsize of 0.03.

Slope

old k's 0.990007 +/- 0.00276351

new k's 0.989845 +/- 0.00276273

This result was surprising to us. Our expectations were that the new method of calculating the relevant quantities will produce better results than the analytical (which assumes Gaussian distribution). But we actually see not significantly different result. The trend is being maintained for a variety of values of the parameters (number of galaxies in the simulation etc.) which implies that the result is universal. The problem could lie in

several things.

a) As the slopes are so similar, but not quite 1, it is possible that there is another aspect of the calculation, that we did not improve.

b) There is an error in the theoretical derivation of the integrals and/or we made some incorrect assumption.

c) There is an error in the code.

The following results show that we may need to be concerned with another issue. By selecting a very small range for the dispersion of the Gaussian of the measurement error we can see if the current estimator (which takes the arithmetic mean of all elipticities) is correct. The issue at hand is that we expect the measurement error to be circularly distributed and thus to even out when the mean is taken. But in elipticity space close to the boundary (magnitudes close to 1) that is certainly not the case. The simulation contains 10^6 galaxies per point. The elipticity probability function is (4.29). Table 4.1 shows the resulting slopes depending on the chosen measurement error.

We observe that for large measurement uncertainties the methods fail to predict the weak lensing shear. Thus we had an idea that it might be plausible to use a new estimator - the arithmetic mean of the elipticities in η-space ($e = \tanh(\eta)$) This requires reevaluation of all integrals needed for the calculation of the relevant quantities in η-space, including the analytical results for $P(e)$ being Gaussian.

4.4 Discussion and conclusion

In this chapter we worked towards a more accurate calculation of a statistical measurement of the applied weak lensing distortion on a set of observed galaxies than

Table 4.1: Table of slopes as a function of measurement error.

Range of σ.	Slope
0.001 - 0.0011	1.00329 $\pm$ 0.00856345
0.005 - 0.0051	1.00342 $\pm$ 0.008485
0.010 - 0.0101	1.00357 $\pm$ 0.00837918
0.050 - 0.0501	1.00411 $\pm$ 0.00775047
0.100 - 0.1001	1.00245 $\pm$ 0.00735592
0.500 - 0.5001	0.82772 $\pm$ 0.0138621
1.000 - 1.0001	0.53667 $\pm$ 0.0195379
2.000 - 2.0001	0.24152 $\pm$ 0.0230548

previously used. Under particular assumptions for the statistical distributions involved, we succeeded in obtaining a simplification of the integral involved, which allowed for significantly faster numerical evaluation. Subsequently we utilized a comparison scheme allowing us to relate the result to analytical formulae used in the literature. The outcome, however, was surprising as it did not show any improvement. We confirmed that the approximation of $P(e)$ being Gaussian is as good as doing the correct integral using the actual $P(e)$ function. Instead we found that the approximation of $p(\mathbf{e}|\tilde{\mathbf{e}})$ may be more problematic. Larger errors led to incorrect Responsivity calculations. While we have an idea that might solve the problem, we did not implement it to test it. Further work would be needed to resolve the situation.

Chapter 5

Conclusion

In chapter 1 we gave an outline of one of the dominant problems in modern cosmology – the nature of Dark Energy. We discussed the issues surrounding an *ad hoc* inclusion of a cosmological constant in the Standard Model and also the difficulties of deriving it from a fundamental theory (like String Theory for example). We pointed out a possible approach for resolving the conundrum – modifying gravity. But as GR is an extremely well tested theory on solar system and laboratory scales ($10^{-3} - 10^{12}m$) any modifications to it must reproduce GR's behavior on small scales. This was very difficult to obtain until the chameleon type models were discovered. These modified theories can change their behavior depending on the environment. Thus, while explaining the current observations on large scales, they can also "evade" observations in dense environments like the solar system.

Testing modifications to gravity is an important and demanding task. We outlined specific characteristics of the large scale structure of the Universe, which, when observed, should provide data allowing us to distinguish between different modifications

or rule some of them out. In particular we focused our attention to the three-point correlation function and spherical collapse. We chose a well developed model in the literature, the $f(R)$ type of modification to gravity.

In chapter 2 we employed perturbation theory in the quasi-linear regime to calculate the deviations of the three point correlation function – the Bispectrum – that would be caused by the $f(R)$ model. We showed that the deviation should have distinct features, but in the physically relevant part of the parameter space of the model and at scales where perturbation theory is applicable, the predicted effect is at the percent level and as such is undetectable by current observations. It does constitute a powerful consistency check of power spectrum measurements. Future surveys, designed to have percent level precision, will be important for testing our predictions.

In chapter 3 we studied the development of a spherical collapse simulation for our $f(R)$ modified gravity model. Spherical collapse has been an important tool in the study of the formation of the large scale structure. A simulation was needed as it was impossible to obtain general analytical solutions for modified gravity, unlike in GR. We described details of our simulation, the technical difficulties and how we chose to resolve them, and finally we presented our first results, which provided a new insight to the issues of non-linearity in gravity. We expect to continue the work with refining our computation and the calculation of additional relevant parameters: virial overdensity, halo mass function etc.

In chapter 4 we focused on the possibility to improve a calculation used in the analysis of weak gravitational lensing. We outlined the traditional way of performing the computation, which uses an approximation of the intrinsic distribution of galaxies

elipticities $P(e)$ by a Gaussian. Then we derived a way of computing the relevant quantity – the Responsivity – for more realistic distributions. The comparison of the two ways of calculating the Responsivity showed that they do not exhibit significant difference, leading to the idea that the approximation of $p(\mathbf{e}|\tilde{\mathbf{e}})$ may be more problematic. Future work should focus on reevaluation of that part of the calculation.

Bibliography

[1] J. Dunkley, et al. 2008, ArXiv e-prints, 803, arXiv:0803.0586

[2] Riess, A. G. et al. 2004, Astrophys. J., 607, 665

[3] G. Dvali, G. Gabadadze, M. Porrati. 2000, Phys.Lett. B, 485, 208; C. Deffayet, 2001, Phys.Lett. B, 502, 199

[4] A. Lue, R. Scoccimarro, G. Starkman, 2004, Phys. Rev. D, 69, 124015

[5] G. Dvali, S. Hofmann, J. Khoury, 2007, Phys. Rev. D, 76, 8, 084006; C. de Rham, S. Hofmann, J. Khoury, A.J. Tolley, 2008, Journal of Cosmology and Astro-Particle Physics, 2, 11, arXiv:0712.2821; C. de Rham, G. Dvali, S. Hofmann, J. Khoury, O. Pujolas, M. Redi, A. J. Tolley, 2008, Phys. Rev. Lett., 100, 251603, arXiv:0711.2072

[6] L. Lombriser, W. Hu, W. Fang, U. Seljak, arXiv:0905.1112

[7] S. M. Carroll, V. Duvvuri, M. Trodden, M. S. Turner, 2004, Phys. Rev. D, 70, 043528; S. M. Carroll, A. De Felice, V. Duvvuri, D. A. Easson, M. Trodden, M. S. Turner, 2005, Phys. Rev. D, 71, 063513; S. Nojiri, S. D. Odintsov, 2007, Int.J.Geom.Meth.Mod.Phys, 4:115

[8] J. Khoury, A. Weltman, 2004, Phys. Rev. D, 69, 044026, astro-ph/0309411v2; 2004, Phys. Rev. Lett., 93, 171104, astro-ph/0309300v3

[9] W. Hu, I. Sawicki, 2007, Phys. Rev. D, 76, 064004, arXiv:0705.1158v1

[10] B. Jain, P. Zhang, 2008, Phys. Rev. D, 78, 063503, arXiv:0709.2375v2

[11] F. Schmidt, M. Lima, H. Oyaizu, W. Hu, 2009, Phys. Rev. D, 79, 8, 083518, arXiv:0812.0545

[12] H. Oyaizu, 2007, Phys. Rev. D, 78, 12, 123523, arXiv:0807.2449v1

[13] M. Bartelmann, P. Schneider, 2001, Phys. Rept., 340, 291

[14] G.M. Bernstein, M. Jarvis, 2002, The Astronomical Journal, 123:583-618.

[15] See, e.g. D. N. Spergel, et al. 2007, ApJS, 170, 377, astro-ph/0603449 M. Tegmark, et al. 2006, Phys. Rev. D, 74, 123507, astro-ph/0608632; A. G. Riess, et al. 2007, Astrophys. J., 659, 98, astro-ph/0611572

[16] M. Milgrom., 1983, Astrophys. J., 207, 371; J. D. Bekenstein, 2004, Phys. Rev. D, 70, 083509

[17] V. Sahni, Y. Shtanov, & A. Viznyuk, 2005, JCAP, 12, 5

[18] M. White, C.S. Kochanek, 2001, Astrophys. J., 560, 539; A. Shirata, T. Shiromizu, N. Yoshida, Y. Suto, 2005, Phys. Rev. D, 71, 064030; C. Sealfon, L. Verde & R. Jimenez, 2005, Phys. Rev. D, 71, 083004; A. Shirata, Y. Suto, C. Hikage, T. Shiromizu, & N. Yoshida, 2007, Phys. Rev. D, 76, 044026, arXiv:0705.1311

[19] C. Frigerio Martins, P. Salucci, 2007 MNRAS, 381, 1103

[20] C. Skordis, D. F. Mota, P. G. Ferreira, C. Boehm, 2006, Phys. Rev. Lett., 96, 011301; C. Skordis, 2006, Phys. Rev. D, 74, 103513

[21] S. Dodelson, M. Liguori, 2006, Phys. Rev. Lett., 97, 231301

[22] L. Knox, Y.-S. Song, J.A. Tyson, 2005, arXiv:astro-ph/0503644; M. Ishak, A. Upadhye, D. N. Spergel, 2006, Phys. Rev. D, 74, 043513

[23] K. Koyama, R. Maartens, 2006, JCAP, 0601, 016

[24] T. Koivisto, H. Kurki-Suonio, 2006, Class.Quant.Grav., 23, 2355-2369; T. Koivisto, 2006, Phys. Rev. D, 73, 083517; B. Li, M.-C. Chu, 2006, Phys. Rev. D, 74, 104010; B. Li & J. Barrow, 2007, Phys. Rev. D, 75, 084010

[25] Y. Song, W. Hu and I. Sawiki, 2006, Phys. Rev. D, 75, 044004, astro-ph/0610532v2

[26] P. Zhang, 2006, Phys. Rev. D, 73, 123504

[27] R. Bean, D. Bernat, L. Pogosian, A. Silvestri, M. Trodden, 2007, Phys. Rev. D, 75, 064020

[28] E. Linder., 2005, Phys. Rev. D, 72, 043529; D. Huterer, E. Linder, 2007, Phys. Rev. D, 75, 023519, astro-ph/0608681

[29] J.-P. Uzan, 2006, arXiv:astro-ph/0605313

[30] R. Caldwell, C., A. Melchiorri, 2007, Phys. Rev. D, 76, 023507, astro-ph/0703375

[31] L. Amendola, M. Kunz, D. Sapone, 2008, Journal of Cosmology and Astro-Particle Physics, 4, 13, arXiv:0704.2421

[32] H. Stabenau, B. Jain, 2006, Phys. Rev. D, 74, 084007

[33] D. Mota, J. Barrow, 2004 MNRAS, 349, 291, astro-ph/0309273

[34] E. Bertschinger , 2006, Astrophys. J., 648, 797

[35] C.-P. Ma, E. Bertschinger, 1995, Astrophys. J.455, 7-25

[36] P. Zhang, M. Liguori, R. Bean, & S. Dodelson, 2007, Phys. Rev. Lett., 99, 141302

[37] W. Hu, I. Sawicki, 2007, Phys. Rev. D, 76, 104043, arXiv:0708.1190v2

[38] M. Amin, R. Wagoner, R. Blandford, 2008, MNRAS, 390, 131-142, arXiv:0708.1793

[39] B. Jain, & E. Bertschinger, 1994, Astrophys. J., 431, 495

[40] H. Oyaizu, M. Lima, W. Hu, 2008, arXiv:0807.2462

[41] F. Bernardeau, 2004, astro-ph/0409224

[42] F. Bernardeau, S. Colombi, E. Gaztañaga, & R. Scoccimarro, 2002, Physics Reports, 367, 1

[43] T. Tatekawa, S. Tsujikawa, 2008, Journal of Cosmology and Astro-Particle Physics, 9, 9, arXiv:0807.2017

[44] E. Sefusatti, M. Crocce, S. Pueblas, & R. Scoccimarro, 2006, Phys. Rev. D, 74, 023522

[45] I. Laszlo, R. Bean, 2008, Phys. Rev. D, 77, 024048

[46] R. Smith, et al, 2003, MNRAS, 341, 1311

[47] R. Scoccimarro, 2008, *in preparation*

[48] M. Martino, H. Stabenau, R. Sheth, 2009, Phys. Rev. D, 79, 8, 084013, arXiv:0812.0200

[49] M. Takada & B. Jain, 2004, MNRAS, 348, 897

[50] P. J. E. Peebles, *The large-scale structure of the universe*, 1980, Princeton University Press. 1980.

[51] W. H. Press, S. A. Teukolsky, W. T. Vetterling, and B. P. Flannery, *Numerical recipes in C. The art of scientific computing* 1992, Cambridge University Press, c1992, 2nd ed.

[52] S. F. Shandrin, 1980, Astrophysics 16, 439.

[53] A. V. Kravtsov, A. A. Klypin, and A. M. Khokhlov, 1997, Astrophys. J. Supplement 111, 73, astro-ph/9701195.

[54] O. Lahav, P. B. Lilje, J. R. Primack, and M. J. Rees, 1991, MNRAS, 251, 128.

[55] V. R. Eke, S. Cole, C. S. Frenk, 1996, MNRAS, 282, 263-280, astro-ph/9601088